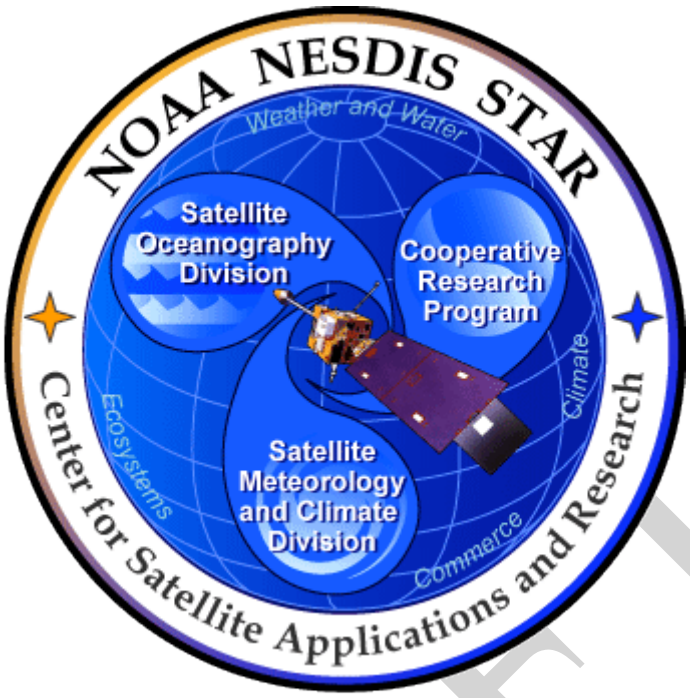

NOAA NESDIS
CENTER for SATELLITE APPLICATIONS and RESEARCH

GOES-R Advanced Baseline Imager (ABI) Algorithm Theoretical Basis Document For Volcanic Ash (Detection and Height)

Michael Pavolonis, NOAA/NESDIS/STAR
Justin Sieglaff, UW-CIMSS

Version 2.0
June 30, 2009

TABLE OF CONTENTS

LIST OF FIGURES

LIST OF TABLES

LIST OF ACRONYMS

ABI – Advanced Baseline Imager
ABI-VAA – Advanced Baseline Imager Volcanic Ash Algorithm
AC – Above Cloud
ATBD – Algorithm Theoretical Basis Document
CALIOP – Cloud-Aerosol Lidar with Orthogonal Polarization
CALIPSO – Cloud-Aerosol Lidar and Infrared Pathfinder Satellite Observation
EOS – Earth Observing System
ESA – European Space Agency
F&PS – Functional & Performance Specification
GOES – Geostationary Operational Environmental Satellite
LRC – Local Radiative Center
MODIS – Moderate Resolution Imaging Spectroradiometer
NASA – National Aeronautics and Space Agency
NESDIS – National Environmental Satellite, Data, and Information Service
NOAA – National Oceanic and Atmospheric Administration
NWP – Numerical Weather Prediction
POES – Polar Operational Environmental Satellite
SEVIRI – Spinning Enhanced Visible and Infrared Imager
SSEC – Space Science and Engineering Center
STAR – Center for Satellite Applications and Research
TOA – Top of Atmosphere

ABSTRACT

The volcanic ash algorithm theoretical basis document (ATBD) provides a high level description of the physical basis for the estimation of cloud height and mass loading (mass per unit area) of volcanic ash clouds observed by the Advanced Baseline Imager (ABI) flown on the GOES-R series of NOAA geostationary meteorological satellites. The generation of these baseline products relies on the ability to determine which pixels potentially contain volcanic ash, so the procedure for determining if there is a high confidence of a given pixel containing volcanic ash is also described.

Pixels that potentially contain volcanic ash are identified using a series of spectral and spatial tests. The detection algorithm utilizes ABI channels 11 (8.5 μm), 14 (11 μm), and 15 (12 μm). In lieu of brightness temperature differences, effective absorption optical depth ratios are used in the spectral tests. Effective absorption optical depth ratios allow for improved sensitivity to cloud microphysics, especially for optically thin clouds. An optimal estimation technique is then applied to all pixels that potentially contain ash in order to estimate the height and mass loading of ash clouds. This retrieval technique utilizes ABI channels 14 (11 μm), 15 (12 μm), and 16 (13.3 μm). While these are difficult products to validate, preliminary comparisons to spaceborne lidar indicate that this approach will likely meet the accuracy requirements.

1 INTRODUCTION

1.1 Purpose of This Document

The volcanic ash algorithm theoretical basis document (ATBD) provides a high level description of the physical basis for the estimation of cloud height and mass loading (mass per unit area) of volcanic ash clouds observed by the Advanced Baseline Imager (ABI) flown on the GOES-R series of NOAA geostationary meteorological satellites. The generation of these baseline products relies on the ability to determine which pixels potentially contain volcanic ash, so the procedure for determining if there is a high confidence of a given pixel containing volcanic ash is also described.

1.2 Who Should Use This Document

The intended user of this document are those interested in understanding the physical basis of the algorithms and how to use the output of this algorithm. This document also provides information useful to anyone maintaining or modifying the original algorithm.

1.3 Inside Each Section

This document is broken down into the following main sections.

- **System Overview**: Provides relevant details of the ABI and provides a brief description of the products generated by the algorithm.
- **Algorithm Description**: Provides all the detailed description of the algorithm including its physical basis, its input and its output.
- **Assumptions and Limitations**: Provides an overview of the current limitations of the approach and gives the plan for overcoming these limitations with further algorithm development.

1.4 Related Documents

- GOES-R Functional & Performance Specification Document (F&PS)
- GOES-R ABI Volcanic Ash Product Validation Plan Document

1.5 Revision History

- 9/30/2008 - Version 1.0 of this document was created by Michael J Pavolonis (NOAA/NESDIS/STAR) and Justin Sieglaff (University of Wisconsin – Madison). Version 1.0 represents the first draft of this document.

- 6/30/2009 – Version 2.0 of this document was created by Michael J Pavolonis (NOAA/NESDIS/STAR) and Justin Sieglaff (University of Wisconsin – Madison). In this revision, Version 1.0 was revised to meet 80% delivery standards.

2 OBSERVING SYSTEM OVERVIEW

This section will describe the products generated by the ABI Volcanic Ash Algorithm (ABI-VAA) and the requirements it places on the sensor.

2.1 Products Generated

The ABI-VAA is responsible for producing an ash cloud height and ash cloud mass loading (mass per unit area) for all ABI pixels that potentially contain volcanic ash. A necessary intermediate product, which describes the confidence of volcanic ash being present for each pixel, is transferred into one of the quality flags.

The ABI volcanic ash products are intended to be used to locate volcanic ash clouds and to initialize and validate ash dispersion models.

2.1.1 Product Requirements

The F&PS spatial, temporal, and accuracy requirements for the GOES-R volcanic ash products are shown below in Table 1.

Name	User & Priority	Geographic Coverage (G, H, C, M)	Vertical Res.	Horiz. Res.	Mapping Accuracy	Msmnt. Rang	Msmnt. Accuracy	Refresh Rate/Coverage Time Option (Mode 3)	Refresh Rate Option (Mode 4)	Data Latency	Long-Term	Product Measurement Precision
Volcanic Ash: detection and height	GOES-R	FD	3 km (top height)	2 km	1 km	0-50 tons/km^2	2 tons/km^2	15 min	5 min	50 sec	TBD	2.5 tons/km^2

Name	User & Priority	Geographic Coverage (G, H, C, M)	Tempral Coverage Qualifiers	Product Extend Qualifiers	Cloud Cover Conditions Qualifiers	Product Statistics Qualifier
Volcanic Ash: detection and height	GOES-R	FD	Day and night	Quantitative out to at least 60 degrees LZA and qualitative beyond	Clear conditions down to feature of interest associated with threshold accuracy	Over volcanic ash cases

Table 1: The GOES-R volcanic ash detection and height requirements.

2.2 Instrument Characteristics

The ABI volcanic ash height and mass loading retrieval will be applied to each pixel determined to have a high confidence of containing volcanic ash as determined by the ash detection component of the algorithm. The final channel set is still being determined as the algorithms are enhanced and validated. Table 1 summarizes the current channels use by the ABI-VAA.

Channel Number	*Wavelength (μm)*	*Used in ABI-VAA*
1	0.47	
2	0.64	
3	0.86	
4	1.38	
5	1.61	
6	2.26	
7	3.9	
8	6.15	
9	7.0	
10	7.4	
11	8.5	✓
12	9.7	
13	10.35	Potential enhancement
14	11.2	✓
15	12.3	✓
16	13.3	✓

Table 1. Channel numbers and wavelengths for the ABI

In general, the ABI-VAA relies on infrared radiances to avoid day/night/terminator discontinuities. Channel 16 provides the needed sensitivity to cloud height for optically thin mid and high level ash clouds while channels 11 and 14-15 provide the needed sensitivity to cloud microphysics (including composition). Note that other ABI channels may be added to future versions of the algorithm to improve performance.

The performance of the ABI-VAA is sensitive to any imagery artifacts or instrument noise. The ABI-VAA expects all observations to be in the form of navigated and calibrated radiances and brightness temperatures. This is critical because the volcanic ash mask compares the observed values to those from a forward radiative transfer model. The channel specifications are given in the F&PS section 3.4.2.1.4.0. We are assuming the performance outlined in this section during our development efforts.

3 ALGORITHM DESCRIPTION

Below is a complete description of the algorithm at the current level of maturity (which will improve with each revision).

3.1 Algorithm Overview

Given the importance of monitoring volcanic ash for aviation interests, health interests, and climate, the ABI-VAA serves a critical role in the GOES-R ABI processing system. Information pertaining to volcanic ash is needed on a very timely basis. As such, latency was a large concern in the development of the ABI-VAA. Given advances made in fast radiative transfer modeling, a state-of-the-art algorithm can be implemented without risking latency issues. The ash cloud height/mass loading retrieval utilizes the same general retrieval procedure as the ABI cloud top height algorithm. Some of the details within the retrieval procedure were modified to accommodate volcanic ash clouds, which, spectrally, behave quite a bit different than meteorological clouds. Given any type of cloud that produces a discernable signal in the infrared, the height/mass loading retrieval will produce an answer. Thus, the application of the retrieval needs to be restricted to pixels that contain volcanic ash clouds. To ensure that this is the case, an ash detection algorithm is applied to all cloudy pixels prior to performing the retrieval. The ash detection algorithm relies on the ABI cloud mask to determine which pixels contain some type of cloud. The ash detection simply determines if the cloud type is volcanic ash. Volcanic ash detection is a very specialized application, so one cannot expect the cloud mask to provide this information.

The ABI-VAA derives the following ABI cloud products listed in the F&PS.

- Ash cloud height [km]
- Ash mass loading [tons/km^2]

Both of these products are derived at the pixel level for all pixels that potentially contain volcanic ash.

In addition, the ABI-VAA derives the following products that are not included in F&PS.

- Quality Flags (including the confidence of volcanic ash being present in a given pixel)

3.2 Processing Outline

As described earlier, the ash height and mass loading retrieval requires *a priori* knowledge of which pixels contain volcanic ash. Thus, prior to calling the ash retrieval algorithm, an ash detection algorithm must be applied to determine which cloudy pixels likely contain volcanic ash. Given this requirement, the algorithm processing precedence is as follows: ABI cloud mask --> ash detection routine --> ash retrieval routine. Both ash routines require multiple scan lines of ABI data due to the spatial analysis that is applied within each. Complete scan line segments should consist of at least 200 scan

lines. Overlap between adjacent scan line segments is useful, but not required for these algorithms. The processing outline of the ash height and mass loading retrieval is summarized in the figure below.

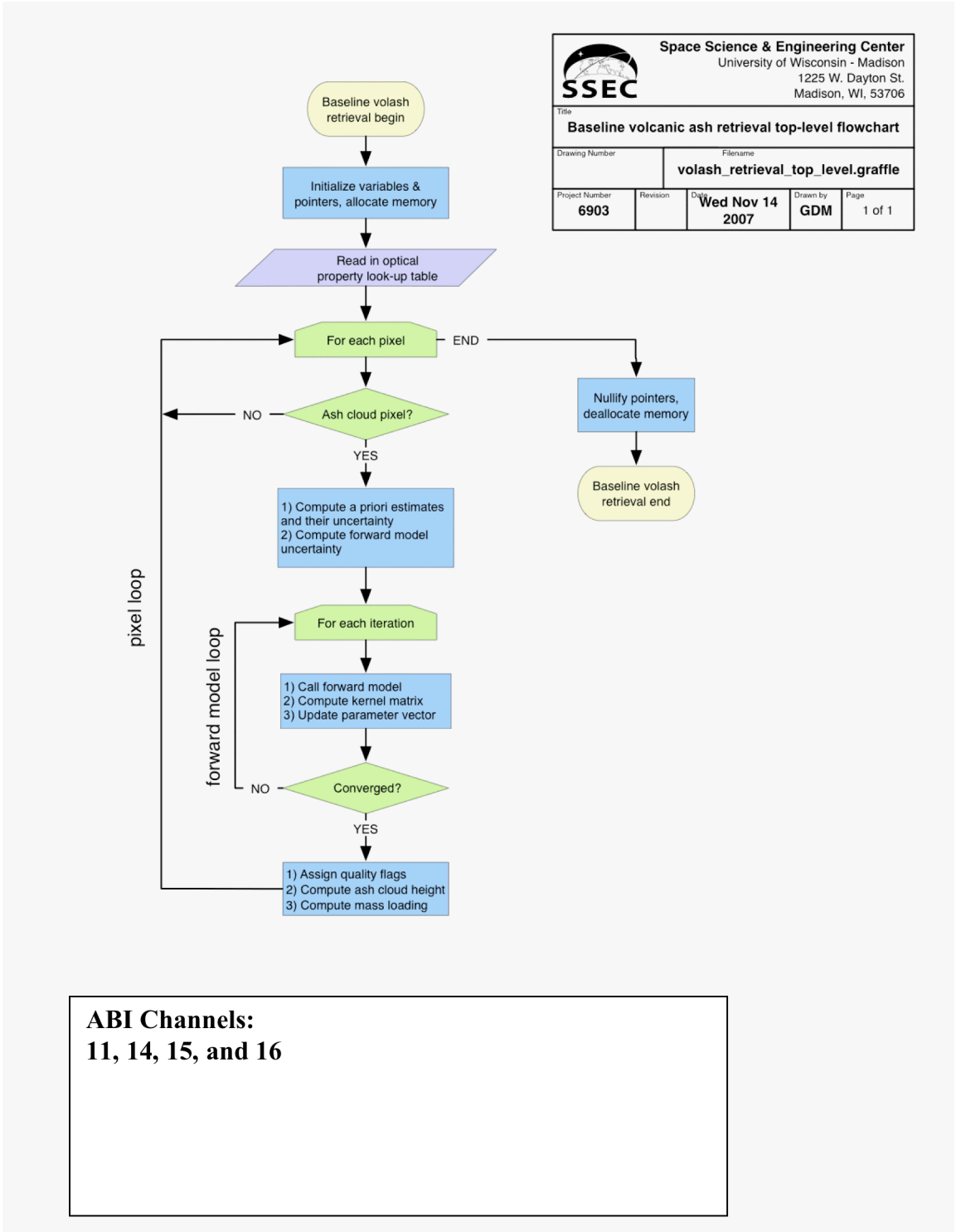

Figure 1: High Level Flowchart of the ABI_VAA illustrating the main processing sections.

3.3 Algorithm Input

This section describes the input needed to process the ABI-VAA. While the ABI-VAA operates on a pixel-by-pixel basis, surrounding pixels are needed for spatial analysis. Therefore, the ABI-VAA must have access to a group of pixels. In its current configuration, we run the ABI-VAA on segments comprised of 200 scan-lines. The following sections describe the actual input needed to run the ABI-VAA.

3.3.1 Primary Sensor Data

The list below contains the primary sensor data currently used by the ABI-VAA. By primary sensor data, we mean information that is derived solely from the ABI observations and geolocation information.

- Calibrated radiances for ABI channels 11, 14, 15 and 16
- Calibrated brightness temperatures for ABI channels 11, 14, 15 and 16
- Sensor viewing zenith angle
- Solar zenith angle
- Relative azimuth angle
- Sensor geolocation (e.g. lat/lon of pixel)
- ABI cloud mask output (product developed by cloud team)

3.3.2 Ancillary Data

The following data lists and briefly describes the ancillary data required to run the ABI-VAA. By ancillary data, we mean data that requires information not included in the ABI observations or geolocation data.

- **Land mask / Surface type**
  A global land cover classification collection created by The University of Maryland Department of Geography (Hansen et al. 1998). Imagery from the AVHRR satellites acquired between 1981 and 1994 were used to distinguish fourteen land cover classes (http://glcf.umiacs.umd.edu/data/landcover/). This product is available at 1 km pixel resolution.

- **Surface emissivity of channels 11, 14, 15 and 16**
  A global database of monthly infrared land surface emissivity derived using input from the Moderate Resolution Imaging Spectroradiometer (MODIS) operational land surface emissivity product (MOD11). Emissivity is available globally at ten wavelengths (3.6, 4.3, 5.0, 5.8, 7.6, 8.3, 9.3, 10.8, 12.1, and 14.3 microns) with 0.05 degree spatial resolution (Seemann et al. 2008). The ten wavelengths serve as anchor points in the linear interpolation to any wavelength between 3.6 and

14.3 microns. The monthly emissivities have been integrated over the ABI spectral response functions to match the ABI channels.

- **Surface temperature**
  Knowledge of the surface temperature is required (Numerical Weather Prediction (NWP) data are used).

- **Profiles of height, pressure and temperature**
  The conversion of cloud-top temperature to cloud-top pressure and height requires knowledge of the atmospheric profiles. Information on the location of the tropopause is also needed. These fields are obtained from NWP output.

3.3.3 Radiative Transfer Models

The following lists and briefly describes the data that must be calculated by a radiative transfer model or derived prior to running the ABI-VAA. The regression-based model, PFAST (Hannon et al., 1996) is used by the ABI-VAA.

- **Clear-sky transmission and radiance profiles for channels 11, 14, 15 and 16**
  The forward model used in the ABI-VAA requires profiles of radiance and transmission relative to the top of the atmosphere along the ABI view angle at high vertical resolution (at least 101 levels). The ABI-VAA uses the 101 levels described in Strow et al. (2003).

- **Clear-sky radiance estimates of channels 11, 14, 15 and 16**
  The ABI-VAA forward model requires knowledge of the radiance ABI would sense under clear-sky conditions.

3.4 Theoretical Description

Important: *These following sub-sections are divided into two parts, one describing the volcanic ash detection methodology, and one describing the volcanic ash height and mass loading retrieval. Some of the physical concepts described in each part will overlap. For the sake of clarity, each part contains a complete description, which results in some redundancy.*

The volcanic ash detection methodology described in this section is based on the physical concepts described in Pavolonis (2009a) and Pavolonis (2009b). The general volcanic ash height and mass loading retrieval methodology is based on the work of Heidinger and Pavolonis (2009).

3.4.1 Physics of the Problem – Volcanic Ash Detection

The volcanic ash detection method utilizes ABI Channels 11, 14, and 15. These channels have an approximate central wavelength of 8.5, 11, and 12 μm, respectively. These central wavelengths will be referred to rather than the ABI channel numbers throughout the "Theoretical Description." The spectral sensitivity to cloud composition is perhaps best understood by examining the imaginary index of refraction, m_i, as a function of wavelength. The imaginary index of refraction is often directly proportional to absorption/emission strength for a given particle composition, in that larger values are indicative of stronger absorption of radiation at a particular wavelength. However, absorption due to photon tunneling, which is proportional to the real index of refraction, can also contribute to the observed spectral absorption under certain circumstances (Mitchell, 2000), but for simplicity, only absorption by the geometrical cross section, which is captured by the imaginary index of refraction, is discussed here. Figure 2 shows m_i for liquid water (Downing and Williams, 1975), ice (Warren and Brandt, 2008), volcanic rock (andesite) (Pollack et al., 1973), and non-volcanic dust (kaolinite) (Roush et al., 1991). While the exact composition, and hence the m_i, of volcanic ash and dust vary depending on the source, andesite and kaolinite were chosen since both minerals exhibit the often exploited "reverse absorption" signature (e.g. Prata, 1989). The "reverse absorption" signature is responsible for the sometimes-observed negative 11 – 12 μm brightness temperature difference associated with volcanic ash and dust.

The m_i can be interpreted as follows. In Figure 2, one sees that around 10 - 11 μm volcanic rock absorbs more strongly than liquid water or ice, while near 12 – 13.5 μm the opposite is true. Thus, all else being equal, the measured brightness temperature by an 12 μm channel will exceed the measured brightness temperature by an 11 μm channel for a volcanic ash cloud, with the opposite being true for a meteorological cloud (e.g. a cloud composed of liquid water and/or ice). The previous statement is only accurate if the meteorological cloud and volcanic ash cloud have the same particle concentrations at the same vertical levels in the same atmosphere, and have the same particle size and shape distribution. That is what is meant by "all else being equal." While Figure 2 is insightful, it can also be deceiving if not interpreted correctly. For example, it is possible that a scene with a meteorological cloud in one type of atmosphere (e.g. contintental mid-latitude) may exhibit the same measured spectral radiance as a scene with an ash cloud in another type of atmosphere (e.g. maritime tropical).

In order to maximize the sensitivity to cloud composition, the information contained in Figure 2 must be extracted from the measured radiances as best as possible. One way of doing this is to account for the background conditions (e.g. surface temperature, surface emissivity, atmospheric temperature, and atmospheric water vapor) of a given scene in an effort to isolate the cloud microphysical signal. This is difficult to accomplish with traditional brightness temperatures and brightness temperature differences. In the following section, we derive a data space that accounts for the background conditions.

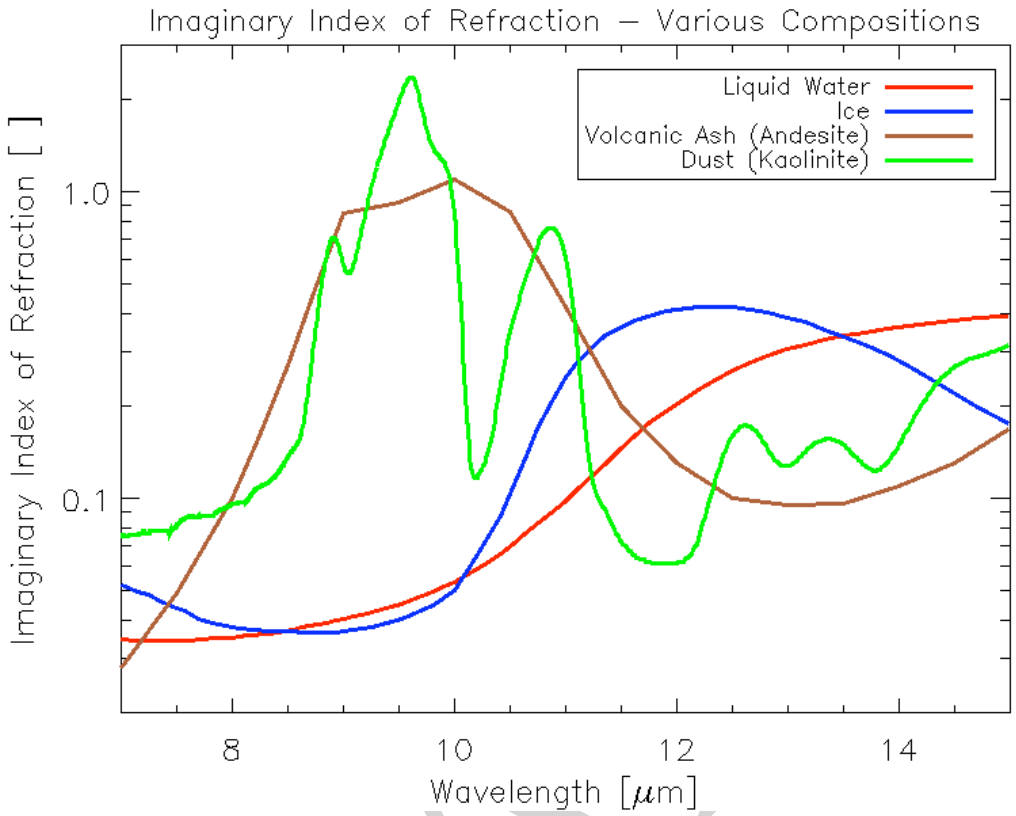

Figure 2: The imaginary index of refraction for liquid water (red), ice (blue), andesite (brown), and kaolinite (green) is shown as a function of wavelength.

3.4.1.1 Infrared Radiative Transfer used in Ash Detection

Assuming a satellite viewing perspective (e.g. upwelling radiation), a fully cloudy field of view, a non-scattering atmosphere (no molecular scattering), and a negligible contribution from downwelling cloud emission or molecular emission that is reflected by the surface and transmitted to the top of troposphere (Zhang and Menzel (2002) showed that this term is very small at infrared wavelengths), the cloudy radiative transfer equation for a given infrared channel or wavelength can be written as in Equation 1 (e.g. Heidinger and Pavolonis, 2009).

$$R_{obs}(\lambda) = \varepsilon(\lambda)R_{ac}(\lambda) + t_{ac}(\lambda)\varepsilon(\lambda)B(\lambda,T_{eff}) + R_{clr}(\lambda)(1-\varepsilon(\lambda)) \quad \text{(Eq. 1)}$$

In Equation 1, λ is wavelength, R_{obs} is the observed radiance, R_{clr} is the clear sky radiance. R_{ac} and t_{ac} are the above cloud upwelling atmospheric radiance and transmittance, respectively. B is the Planck Function, and T_{eff} is the effective cloud temperature. The estimation of the clear sky radiance and transmittance will be explained later on in this section. The effective cloud emissivity (Cox, 1976) is given by ε. To avoid using additional symbols, the angular dependence is simply implied.

Equation 1 can readily be solved for the effective cloud emissivity as follows:

$$\varepsilon(\lambda) = \frac{R_{obs}(\lambda) - R_{clr}(\lambda)}{[B(\lambda, T_{eff})t_{ac}(\lambda) + R_{ac}(\lambda)] - R_{clr}(\lambda)} \quad \text{(Eq. 2)}$$

In Equation 2, the term in brackets in the denominator is the blackbody cloud radiance that is transmitted to the top of atmosphere (TOA) plus the above cloud (ac) atmospheric radiance. This term is dependent upon the effective cloud vertical location. This dependence will be discussed in detail in later sections.

The cloud microphysical signature cannot be captured with the effective cloud emissivity alone for a given spectral channel or wavelength. It is the spectral variation of the effective cloud emissivity that holds the cloud microphysical information. To harness this information, the effective cloud emissivity is used to calculate effective absorption optical depth ratios; otherwise known as β-ratios (see Inoue 1987; Parol et al., 1991; Giraud et al., 1997; and Heidinger and Pavolonis, 2009). For a given pair of spectral emissivities ($\varepsilon(\lambda_1)$ and $\varepsilon(\lambda_2)$):

$$\beta_{obs} = \frac{\ln[1 - \varepsilon(\lambda_1)]}{\ln[1 - \varepsilon(\lambda_2)]} = \frac{\tau_{abs}(\lambda_1)}{\tau_{abs}(\lambda_2)} \quad \text{(Eq. 3)}$$

Notice that Equation 3 can simply be interpreted as the ratio of effective absorption optical depth (τ) at two different wavelengths. The word "effective" is used since the cloud emissivity depends upon the effective cloud temperature. The effective cloud temperature is most often different from the thermodynamic cloud top temperature since the cloud emission originates from a layer in the cloud. The depth of this layer depends upon the cloud transmission profile, which is generally unknown. One must also consider that the effects of cloud scattering are implicit in the cloud emissivity calculation since the actual observed radiance will be influenced by cloud scattering to some degree. In other words, no attempt is made to separate the effects and absorption and scattering. At wavelengths in the 10 to 13 μm range, the effects of cloud scattering for upwelling radiation are quite small and usually negligible. But at infrared wavelengths in the 8 – 10 μm range, the cloud reflectance can make a 1 – 3% contribution to the top of atmosphere radiance (Turner, 2005). Thus, it is best to think of satellite-derived effective cloud emissivity as a radiometric parameter, which, in most cases, is proportional to the fraction of radiation incident on the cloud base that is absorbed by the cloud. See Cox (1976) for an in depth explanation of effective cloud emissivity.

An appealing quality of β_{obs}, is that it can be interpreted in terms of the single scatter properties, which can be computed for a given cloud composition and particle distribution. Following Van de Hulst (1980) and Parol et al. (1991), a spectral ratio of scaled extinction coefficients can be calculated from the single scatter properties (single scatter albedo, asymmetry parameter, and extinction cross section), as follows.

$$\beta_{theo} = \frac{[1.0 - \omega(\lambda_1)g(\lambda_1)]\sigma_{ext}(\lambda_1)}{[1.0 - \omega(\lambda_2)g(\lambda_2)]\sigma_{ext}(\lambda_2)} \quad \text{(Eq. 4)}$$

In Equation 4, β_{theo} is the spectral ratio of scaled extinction coefficients, ω is the single scatter albedo, g is the asymmetry parameter, and σ_{ext} is the extinction cross section. At wavelengths in the 8 – 15 μm range, where multiple scattering effects are small, β_{theo}, captures the essence of the cloudy radiative transfer such that,

$$\beta_{obs} \approx \beta_{theo} \quad \text{(Eq. 5)}$$

Equation 4, which was first shown to be accurate for observation in the 10 – 12 μm "window" by Parol et al. (1991), only depends upon the single scatter properties. It does not depend upon the observed radiances, cloud height, or cloud optical depth. By using β-ratios as opposed to brightness temperature differences, we are not only accounting for the non-cloud contribution to the radiances, we are also providing a means to tie the observations back to theoretical size distributions. This framework clearly has practical and theoretical advantages over traditional brightness temperature differences. Parol et al. (1991) first showed that Equation 5 is a good approximation. Since that time, faster computers and improvements in the efficiency and accuracy of clear sky radiative transfer modeling have allowed for more detailed exploration of the β data space and computation of β-ratios on a global scale. As such, Pavolonis (2009a) and Pavolonis (2009b) showed that β-ratios offer improved sensitivity to the presence of volcanic ash relative to brightness temperature differences for the same channel pair.

3.4.1.2 Cloud Composition Differences in β-Space

Two channel pairs are used in the volcanic ash detection algorithm, the 8.5, 11 μm pair (ABI Channels 11 and 14) and the 11, 12 μm pair (ABI Channels 14 and 15). From these channel pairs, β-ratios were constructed such that the 11 μm channel is always placed in the denominator of Equations 3 and 4. Hereafter, these β's are referred to as β(8.5/11μm) and β(12/11μm). The single scatter property relationship (Equation 4) can be used to establish a theoretical relationship for these β's as a function of cloud composition and cloud particle size. Figure 3 shows the relationship between β(8.5/11μm) and β(12/11μm) as given by the single scatter properties (see Equation 4) for various cloud compositions with a varying effective particle radius. With the exception of ice, all single scatter properties were calculated using Mie theory. The ice single scatter properties were taken from the Yang et al. (2005) database, assuming a plate habit. Our analysis of the Yang et al. (2005) database indicates that the sensitivity to particle habit is small compared to the sensitivity to composition and particle size, so only a single ice habit is shown for the sake of clarity. From this figure, one can see that separating meteorological cloud from ash or dust clouds can be effectively accomplished using a tri-spectral (8.5, 11, 12 μm) technique. Differentiating between ash and dust, however, requires additional information. Unlike brightness temperature differences, these β relationships are only a function of the cloud microphysical properties.

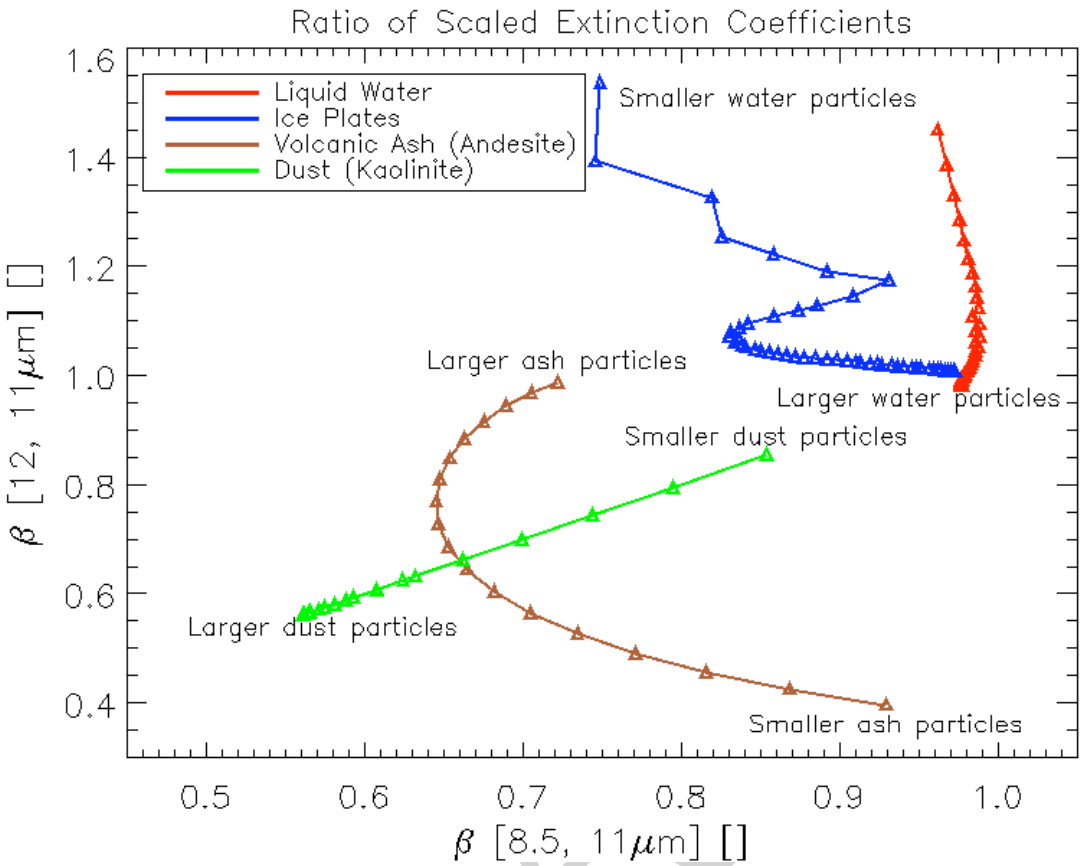

Figure 3: The 12/11 μm scaled extinction ratio (β(12/11μm)) is shown as a function of the 8.5/11 μm scaled extinction ratio (β(8.5/11μm)) for liquid water spheres (red), ice plates (blue), andesite spheres (brown), and kaolinite spheres (green). A range of particle sizes is shown for each composition. For liquid water and ice, the effective particle radius was varied from 5 to 54 μm. The andesite and kaolinite effective particle radius was varied from 1 to 12 μm. The large and small particle ends of each curve are labeled. These β-ratios were derived from the single scatter properties.

3.4.2 Mathematical Description – Volcanic Ash Detection

3.4.2.1 Converting the Measured Radiances to Emissivities and β-Ratios

Given the measured radiances at 8.5, 11, and 12 μm (ABI channels 11, 14, and 15) and estimates of the clear sky radiance, clear sky transmittance, and the temperature profile, Equations 2 and 3 are used to compute β for the 8.5, 11 μm pair and the 11, 12 μm pair, where the 11 μm emissivity is always placed in the denominator of Equation 3. Hereafter, these β's are referred to as β(8.5/11μm) and β(12/11μm). The only missing piece of information is the effective cloud vertical level, which is needed in computing the cloud emissivity. As shown in Pavolonis (2009a) and Pavolonis (2009b), the

sensitivity of β to the effective cloud vertical level is small when "window" channel pairs are used. As such, a constant cloud vertical level can be assumed. In the ABI volcanic ash detection approach, three different cloud vertical level formulations, which are described in Pavolonis (2009a), are applied to Equation 2. The first assumes a constant cloud level consistent with the thermodynamic tropopause given by numerical weather prediction (NWP) data. Equations 6a - 6e specifically shows how this assumption is applied to Equations 2 and 3 for the channel pairs used in the ash detection scheme. In these equations, $\varepsilon_{tropo}(\lambda)$ is the spectral cloud emissivity computed using the tropopause assumption, and $\beta_{tropo}(\lambda_1/\lambda_2)$ represents the β calculated from this type of cloud emissivity. T_{tropo} is the temperature of the tropopause. $R_{tropo}(\lambda)$ and $t_{tropo}(\lambda)$ are the clear sky atmospheric radiance and transmittance, vertically integrated from the tropopause to the top of the atmosphere, respectively. All other terms were defined previously.

$$\varepsilon_{tropo}(8.5\mu m) = \frac{R_{obs}(8.5\mu m) - R_{clr}(8.5\mu m)}{[B(8.5\mu m, T_{tropo})t_{tropo}(8.5\mu m) + R_{tropo}(8.5\mu m)] - R_{clr}(8.5\mu m)} \quad \text{(Eq. 6a)}$$

$$\varepsilon_{tropo}(11\mu m) = \frac{R_{obs}(11\mu m) - R_{clr}(11\mu m)}{[B(11\mu m, T_{tropo})t_{tropo}(11\mu m) + R_{tropo}(11\mu m)] - R_{clr}(11\mu m)} \quad \text{(Eq. 6b)}$$

$$\varepsilon_{tropo}(12\mu m) = \frac{R_{obs}(12\mu m) - R_{clr}(12\mu m)}{[B(12\mu m, T_{tropo})t_{tropo}(12\mu m) + R_{tropo}(12\mu m)] - R_{clr}(12\mu m)} \quad \text{(Eq. 6c)}$$

$$\beta_{tropo}(8.5/11\mu m) = \frac{\ln[1 - \varepsilon_{tropo}(8.5\mu m)]}{\ln[1 - \varepsilon_{tropo}(11\mu m)]} \quad \text{(Eq. 6d)}$$

$$\beta_{tropo}(12/11\mu m) = \frac{\ln[1 - \varepsilon_{tropo}(12\mu m)]}{\ln[1 - \varepsilon_{tropo}(11\mu m)]} \quad \text{(Eq. 6e)}$$

The second cloud vertical level formulation assumes that the cloud vertical level is the level where the atmospheric temperature (given by NWP) is equal to the 11 μm brightness temperature minus 5 K. Equations 7a - 7e specifically shows how this assumption is applied to Equations 2 and 3 for the channel pairs used in the ash detection scheme. In these equations, $\varepsilon_{t5}(\lambda)$ is the spectral cloud emissivity computed using this assumption, and $\beta_{t5}(\lambda_1/\lambda_2)$ represents the β calculated from this type of cloud emissivity. T_{t5} is the 11 μm brightness temperature minus 5 K (BT(11μm) – 5K). $R_{t5}(\lambda)$ and $t_{t5}(\lambda)$ are the clear sky atmospheric radiance and transmittance, vertically integrated from the level where the atmospheric temperature is equal to the [BT(11μm) – 5K] to the top of the atmosphere, respectively. All other terms were defined previously.

$$\varepsilon_{t5}(8.5\mu m) = \frac{R_{obs}(8.5\mu m) - R_{clr}(8.5\mu m)}{[B(8.5\mu m, T_{t5})t_{t5}(8.5\mu m) + R_{t5}(8.5\mu m)] - R_{clr}(8.5\mu m)} \quad \text{(Eq. 7a)}$$

$$\varepsilon_{t5}(11\mu m) = \frac{R_{obs}(11\mu m) - R_{clr}(11\mu m)}{[B(11\mu m, T_{t5})t_{t5}(11\mu m) + R_{t5}(11\mu m)] - R_{clr}(11\mu m)} \quad \text{(Eq. 7b)}$$

$$\varepsilon_{t5}(12\mu m) = \frac{R_{obs}(12\mu m) - R_{clr}(12\mu m)}{[B(12\mu m, T_{t5})t_{t5}(12\mu m) + R_{t5}(12\mu m)] - R_{clr}(12\mu m)} \quad \text{(Eq. 7c)}$$

$$\beta_{t5}(8.5/11\mu m) = \frac{\ln[1-\varepsilon_{t5}(8.5\mu m)]}{\ln[1-\varepsilon_{t5}(11\mu m)]} \quad \text{(Eq. 7d)}$$

$$\beta_{t5}(12/11\mu m) = \frac{\ln[1-\varepsilon_{t5}(12\mu m)]}{\ln[1-\varepsilon_{t5}(11\mu m)]} \quad \text{(Eq. 7e)}$$

The third cloud vertical level formulation assumes that the cloud vertical level is the level where the atmospheric temperature (given by NWP) is equal to the 11 μm brightness temperature minus 10 K. This formulation includes an additional twist. In this formulation, the clear sky top-of-atmosphere radiance is replaced with the top-of-atmosphere radiance originating from a black (e.g. emissivity = 1.0 at all wavelengths) elevated surface. The black surface is placed at the 0.8 sigma level in a terrain following coordinate system. The pressure level (P_{black}) of this black surface is given by Equation 8. In Equation 8, $\sigma = 0.8$, $P_{surface}$ is the surface pressure (from NWP), and P_{toa} is the pressure at the highest level in the profile (from NWP). This type of coordinate system is commonly used in dynamical models. The purpose of this formulation is to help detect ash clouds that overlap lower meteorological clouds. Equations 9a - 9e specifically shows how this assumption is applied to Equations 2 and 3 for the channel pairs used in the ash detection scheme. In these equations, $\varepsilon_{t10}(\lambda)$ is the spectral cloud emissivity computed using this formulation, and $\beta_{t10}(\lambda_1/\lambda_2)$ represents the β calculated from this type of cloud emissivity. T_{t10} is the 11 μm brightness temperature minus 10 K (BT(11μm) – 10K). $R_{t10}(\lambda)$ and $t_{t10}(\lambda)$ are the clear sky atmospheric radiance and transmittance, vertically integrated from the level where the atmospheric temperature is equal to the [BT(11μm) – 10K] to the top of the atmosphere, respectively. T_{black} is the temperature at the pressure level, P_{black}. $R_{black}(\lambda)$ and $t_{black}(\lambda)$ are the clear sky atmospheric radiance and transmittance, vertically integrated from the level where the atmospheric pressure is equal to P_{black} to the top of the atmosphere, respectively. All other terms were defined previously.

$$P_{black} = (P_{surface} - P_{toa})\sigma + P_{toa} \quad \text{(Eq. 8)}$$

$$\varepsilon_{t10}(8.5\mu m) = \frac{R_{obs}(8.5\mu m) - [B(8.5\mu m, T_{black})t_{black}(8.5\mu m) + R_{black}(8.5\mu m)]}{[B(8.5\mu m, T_{t10})t_{t10}(8.5\mu m) + R_{t10}(8.5\mu m)] - [B(8.5\mu m, T_{black})t_{black}(8.5\mu m) + R_{black}(8.5\mu m)]} \quad \text{(Eq. 9a)}$$

$$\varepsilon_{t10}(11\mu m) = \frac{R_{obs}(11\mu m) - [B(11\mu m, T_{black})t_{black}(11\mu m) + R_{black}(11\mu m)]}{[B(11\mu m, T_{t10})t_{t10}(11\mu m) + R_{t10}(11\mu m)] - [B(11\mu m, T_{black})t_{black}(11\mu m) + R_{black}(11\mu m)]} \quad \text{(Eq. 9b)}$$

$$\varepsilon_{t10}(12\mu m) = \frac{R_{obs}(12\mu m) - [B(12\mu m, T_{black})t_{black}(12\mu m) + R_{black}(12\mu m)]}{[B(12\mu m, T_{t10})t_{t10}(12\mu m) + R_{t10}(12\mu m)] - [B(12\mu m, T_{black})t_{black}(12\mu m) + R_{black}(12\mu m)]}$$

(Eq. 9c)

$$\beta_{t10}(8.5/11\mu m) = \frac{\ln[1 - \varepsilon_{t10}(8.5\mu m)]}{\ln[1 - \varepsilon_{t10}(11\mu m)]} \quad \text{(Eq. 9d)}$$

$$\beta_{t10}(12/11\mu m) = \frac{\ln[1 - \varepsilon_{t10}(12\mu m)]}{\ln[1 - \varepsilon_{t10}(11\mu m)]} \quad \text{(Eq. 9e)}$$

A set of rules is later applied to the radiative parameters computed from these formulations. Prior to describing these rules, the use of spatial information in the ash detection scheme must be explained.

3.4.2.2 Identifying a Pixel's Local Radiative Center

In regions where the radiative signal of an ash cloud is small, like cloud edges, the various β-ratios are difficult to interpret since the cloud fraction, which is assumed to be 1.0, may be less than 1.0, or very small cloud optical depths may produce a signal that cannot be differentiated from noise. With the spectral information limited, a spatial metric is needed to make a spatially and physically consistent ash/no ash determination for these types of pixels. Each pixel with an $\varepsilon_{tropo}(11\mu m) < 0.7$ (see Equation 6b) is assigned a corresponding Local Radiative Center (LRC) pixel. Pixels with $\varepsilon_{tropo}(11\mu m) \geq 0.7$ are indicative of a very strong cloud radiative signal, so no spatial information is needed for these pixels.

The LRC for each pixel is determined as follows. Given a $\varepsilon_{tropo}(11\mu m)$ image, the LRC for a given pixel is defined as the pixel location in the direction of the gradient vector upon which the gradient reverses or when an emissivity value ($\varepsilon_{tropo}(11\mu m)$) greater than or equal to 0.7 is found, whichever occurs first. The gradient vector points from low to high $\varepsilon_{tropo}(11\mu m)$ pixels such that it is perpendicular to isolines of $\varepsilon_{tropo}(11\mu m)$. For a given pixel, all eight adjacent pixels are examined to determine which direction the gradient vector points. This concept is best illustrated with a figure. Figure 4 shows an actual gradient vector field, which has been thinned for the sake of clarity. As can be seen, the vectors in this image point from cloud edge towards the optically thicker interior of the cloud. This allows one to consult the spectral information at an interior pixel within the same cloud in order to avoid using the spectral information offered by pixels with a very weak cloud radiative signal. Overall, this use of spatial information allows for a more spatially and physically consistent product. This concept is explained in detail in Pavolonis (2009b).

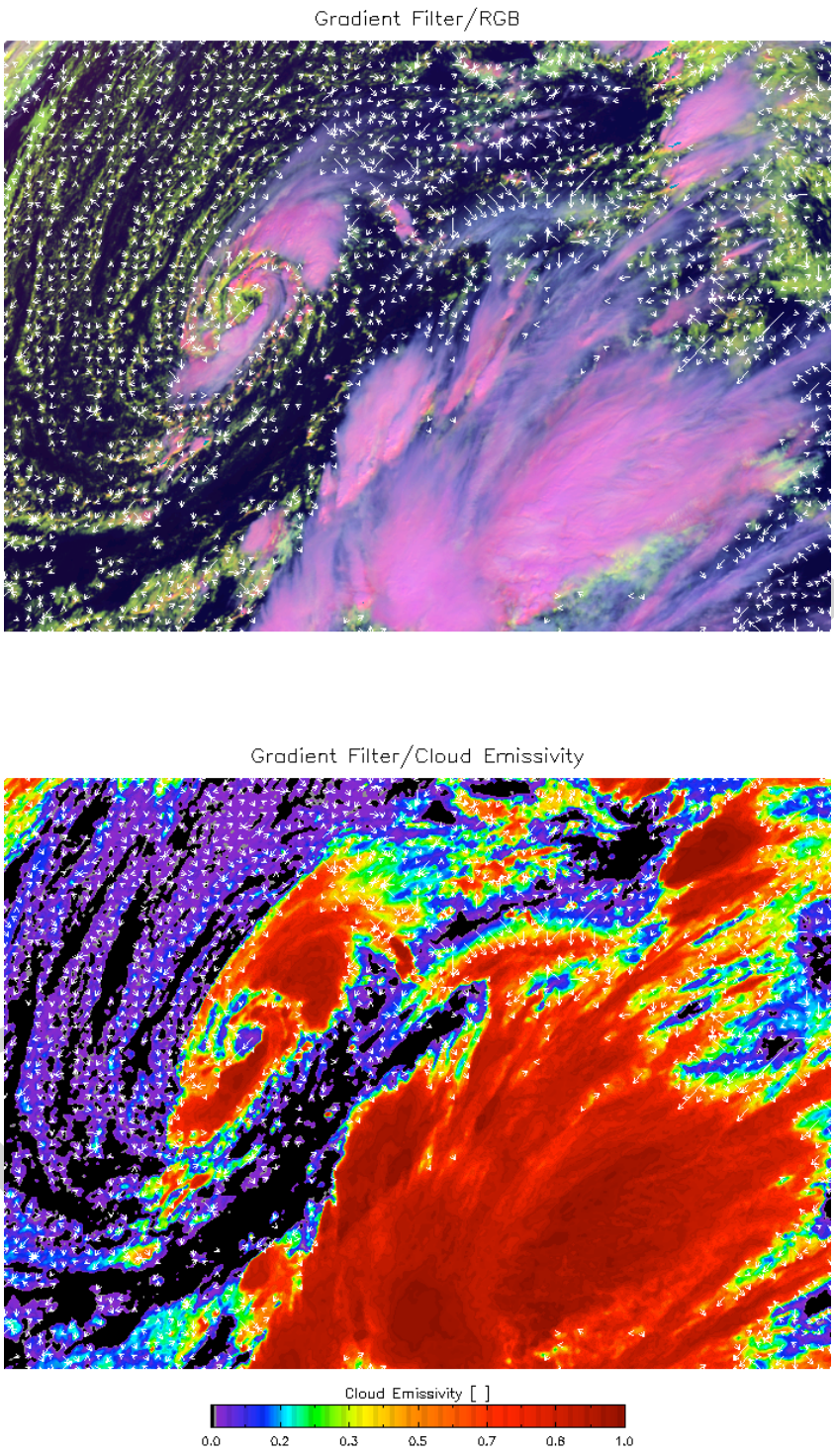

Figure 4: The gradient vector with respect to cloud emissivity at the top of the troposphere is shown overlaid on a false color RGB image (top) and the actual cloud emissivity image itself (bottom). The tail of the arrow indicates the reference pixel location, while the head indicates the Local Radiative Center (LRC) of that reference pixel. For clarity, the vector field has been thinned.

3.4.2.3 Volcanic Ash Detection Rules

Volcanic ash detection is performed by applying rules to the radiative parameters derived in the previous sections. These rules are as follows.

1. Only pixels flagged as cloudy by the ABI cloud mask can potentially contain volcanic ash. The cloud mask does not provide information on cloud type, so additional rules are needed to determine which cloudy pixels contain volcanic ash.

2. Only pixels with a $\varepsilon_{tropo}(11\mu m) > 0.02$ (see Equation 6b) can contain volcanic ash. This rule ensures that the ash/no ash decision is based on a minimum radiative signal.

3. The $\beta_{t5}(8.5/11\mu m)$ and $\beta_{t5}(12/11\mu m)$ (see Equations 7d and 7e) at each pixel, that meets the criteria outlined in the first two rules, is used to assign an ash confidence flag of 0, 1, 3, or 5. Lower values indicate greater confidence. Confidence is measured by how closely $\beta_{t5}(8.5/11\mu m)$ and $\beta_{t5}(12/11\mu m)$ match the theoretical ash cloud values (given by Equation 4) for the same channel combinations. These theoretical values are shown in Figure 3. Each confidence value has the following meaning.

    - Confidence flag = 0:
        - $[\beta_{t5}(8.5/11\mu m) \geq 0.10$ AND $\beta_{t5}(8.5/11\mu m) \leq 0.80$ AND $\beta_{t5}(12/11\mu m) \geq 0.10$ AND $\beta_{t5}(12/11\mu m) < 1.00]$ OR $[\beta_{t5}(8.5/11\mu m) > 0.80$ AND $\beta_{t5}(8.5/11\mu m) \leq 0.90$ AND $\beta_{t5}(12/11\mu m) \geq 0.10$ AND $\beta_{t5}(12/11\mu m) < 0.80]$ OR $[\beta_{t5}(8.5/11\mu m) > 0.90$ AND $\beta_{t5}(12/11\mu m) \geq 0.10$ AND $\beta_{t5}(12/11\mu m) < 0.40]$

    - Confidence flag = 1:
        - $[\beta_{t5}(8.5/11\mu m) > 0.80$ AND $\beta_{t5}(8.5/11\mu m) \leq 0.90$ AND $\beta_{t5}(12/11\mu m) \geq 0.80$ AND $\beta_{t5}(12/11\mu m) < 0.95]$ OR $[\beta_{t5}(8.5/11\mu m) > 0.90$ AND $\beta_{t5}(12/11\mu m) \geq 0.40$ AND $\beta_{t5}(12/11\mu m) < 0.50]$

    - Confidence flag = 3:
        - $[\beta_{t5}(8.5/11\mu m) > 0.80$ AND $\beta_{t5}(8.5/11\mu m) \leq 0.90$ AND $\beta_{t5}(12/11\mu m) \geq 0.95$ AND $\beta_{t5}(12/11\mu m) < 1.00]$ OR $[\beta_{t5}(8.5/11\mu m) > 0.90$ AND $\beta_{t5}(12/11\mu m) \geq 0.50$ AND $\beta_{t5}(12/11\mu m) < 0.60]$

    - Confidence flag = 5:
        - Any other combinations for $\beta_{t5}(8.5/11\mu m)$ and $\beta_{t5}(12/11\mu m)$

4. For pixels with a $\varepsilon_{tropo}(11\mu m) < 0.7$, Rule #3 is repeated using $\beta_{t5}(8.5/11\mu m)$ and $\beta_{t5}(12/11\mu m)$ at the pixel's local radiative center. If $\varepsilon_{tropo}(11\mu m) > 0.7$, a confidence flag of 0 is assigned.

5. If the sum of the confidence flag determined from Rules 3 and 4 is < 6, then the pixel contains volcanic ash.

6. Rules 3 - 5 are repeated using $\beta_{t10}(8.5/11\mu m)$ and $\beta_{t10}(12/11\mu m)$ to better detect volcanic ash clouds that overlap lower meteorological clouds.

3.4.2.4 Noise Filtering

In an effort to eliminate isolated volcanic ash false alarms, the volcanic ash mask, constructed using the rules described in Section 3.4.2.3, is subjected to a standard median filter that is applied to 3 x 3 pixel arrays centered on the pixel of interest. The median filter simply replaces the value at each pixel with the median value of a 3 x 3 pixel array centered on that pixel. Figure 5 shows the impact of the median filter. The median filter is very effective at eliminating random incoherent false alarms, which are similar to "salt and pepper" noise.

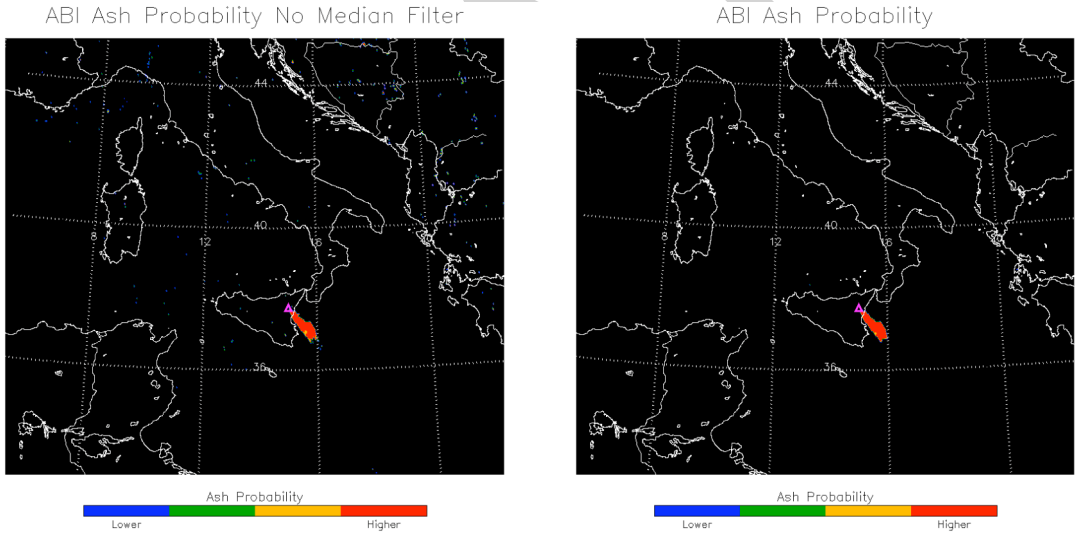

Figure 5: Volcanic ash confidence is shown for an eruption of Etna. The image on the left shows the results without the median filter applied. The image on the right shows the results with the median filter applied. The median filter eliminates isolated false alarms (blue speckles), while leaving the actual volcanic ash cloud in tact (orange/red feature).

3.4.2.5 Ash/Dust Discrimination

Figure 2 and Figure 3 show that volcanic rock and desert dust have similar spectral signatures in the 8 – 12 μm "window." Thus, most airborne dust clouds will be detected

by the volcanic ash detection scheme. While detecting dust clouds is certainly important, the goal of the ABI volcanic ash algorithm is to isolate volcanic ash clouds. Thus, it is desirable to indicate, via a quality flag, when dust, not ash, is likely present. The methodology used to discriminate ash from dust is still being developed, but it is based on the property that dust clouds are most often more spatially uniform in 11-μm brightness temperature than ash clouds. The next version of the ATBD will elaborate on this topic.

3.4.3 Physics of the Problem – Volcanic Ash Retrieval

The volcanic ash retrieval algorithm utilizes ABI channels 14, 15, and 16 (11 μm, 12 μm, and 13.3 μm). These channels are referred to by their approximate central wavelengths (11 μm, 12 μm, and 13.3 μm) throughout this "Theoretical Description." The algorithm does not directly retrieve ash height or ash mass loading. It retrieves ash cloud effective temperature, effective emissivity, and a microphysical parameter. These retrieved parameters are then used to estimate the ash cloud height and mass loading.

3.4.3.1 Cloudy Radiative Transfer

Assuming a satellite viewing perspective (e.g. upwelling radiation), a fully cloudy field of view, a non-scattering atmosphere (no molecular scattering), and a negligible contribution from downwelling cloud emission or molecular emission that is reflected by the surface and transmitted to the top of troposphere (Zhang and Menzel (2002) showed that this term is very small at infrared wavelengths), the cloudy radiative transfer equation for a given infrared channel or wavelength can be written as in Equation 10 (e.g. Heidinger and Pavolonis, 2009).

$$R_{obs}(\lambda) = \varepsilon(\lambda)R_{ac}(\lambda) + t_{ac}(\lambda)\varepsilon(\lambda)B(\lambda,T_{eff}) + R_{clr}(\lambda)(1-\varepsilon(\lambda)) \quad \text{(Eq. 10)}$$

In Equation 10, λ is wavelength, R_{obs} is the observed radiance, R_{clr} is the clear sky radiance. R_{ac} and t_{ac} are the above cloud upwelling atmospheric radiance and transmittance, respectively. B is the Planck Function, and T_{eff} is the effective cloud temperature. The effective cloud emissivity (Cox, 1976) is given by ε. To avoid using additional symbols, the angular dependence is simply implied. While the above radiative transfer equation is simple in that it does not explicitly account for cloud scattering (cloud scattering is implicitly accounted for in the effective emissivity, see Cox, 1976) and that the cloud can be treated as a single layer, it does allow for semi-analytic derivations of the observations to the controlling parameters (i.e. cloud temperature). This is critical because it allows for an efficient retrieval without the need for large lookup tables.

Equation 10 can readily be solved for the effective cloud emissivity as follows:

$$\varepsilon(\lambda) = \frac{R_{obs}(\lambda) - R_{clr}(\lambda)}{[B(\lambda, T_{eff})t_{ac}(\lambda) + R_{ac}(\lambda)] - R_{clr}(\lambda)} \quad \text{(Eq. 11)}$$

In Equation 11, the term in brackets in the denominator is the blackbody cloud radiance that is transmitted to the top of atmosphere (TOA) plus the above cloud (ac) atmospheric radiance. This term is dependent upon the cloud vertical location.

In this retrieval algorithm, the effective cloud emissivity is allowed to vary spectrally. It is the spectral variation of the effective cloud emissivity that holds the cloud microphysical information (particle size, shape, and composition), which is important for calculating the ash mass loading. To account for this spectral variation, the effective cloud emissivity is used to calculate effective absorption optical depth ratios; otherwise known as β-ratios (see Inoue 1987; Parol et al., 1991; Giraud et al., 1997; and Heidinger and Pavolonis, 2009). For a given pair of spectral cloud emissivities ($\varepsilon(\lambda_1)$ and $\varepsilon(\lambda_2)$):

$$\beta_{obs} = \frac{\ln[1 - \varepsilon(\lambda_1)]}{\ln[1 - \varepsilon(\lambda_2)]} = \frac{\tau_{abs}(\lambda_1)}{\tau_{abs}(\lambda_2)} \quad \text{(Eq. 12)}$$

Notice that Equation 12 can simply be interpreted as the ratio of effective absorption optical depth (τ) at two different wavelengths or channels. Allowing the ash cloud microphysics to vary will also allow for improved estimates of ash cloud height as well.

An appealing quality of β_{obs}, is that it can be interpreted in terms of the single scatter properties, which can be computed for a given cloud composition and particle distribution. Following Van de Hulst (1980) and Parol et al. (1991), a spectral ratio of scaled extinction coefficients can be calculated from the single scatter properties (single scatter albedo, asymmetry parameter, and extinction cross section), as follows.

$$\beta_{theo} = \frac{[1.0 - \omega(\lambda_1)g(\lambda_1)]\sigma_{ext}(\lambda_1)}{[1.0 - \omega(\lambda_2)g(\lambda_2)]\sigma_{ext}(\lambda_2)} \quad \text{(Eq. 13)}$$

In Equation 13, β_{theo} is the spectral ratio of scaled extinction coefficients, ω is the single scatter albedo, g is the asymmetry parameter, and σ_{ext} is the extinction cross section. At wavelengths in the 8 – 15 μm range, where multiple scattering effects are small, β_{theo}, captures the essence of the cloudy radiative transfer such that,

$$\beta_{obs} \approx \beta_{theo} \quad \text{(Eq. 14)}$$

Equation 14, which was first shown to be accurate for observation in the 10 – 12 μm "window" by Parol et al. (1991), only depends upon the single scatter properties. This relationship is also verified in Pavolonis (2009a).

3.4.3.2 Microphysical Relationships

Since the ash retrieval utilizes three channels, two different β_{obs} are required to describe the spectral variation of cloud emissivity. Unfortunately, imager measurements do not contain enough information to retrieve more than one β_{obs}, so a pre-established relationship between the two β_{obs} must be used to constrain the retrieval problem. More specifically, the ash composition (e.g. the type of rock) and the ash particle habit (e.g. shape) must be assumed. This constraint, however, does not prevent the retrieval of quality ash particle size information. This pre-established relationship is derived from the corresponding spectral ratio of scaled extinction coefficients, as defined by Equation 13. All of the necessary microphysical assumptions are described below.

The volcanic ash particles are taken to be composed of andesite (Pollack et al, 1973). The size distribution was assumed to be lognormal. Lognormal distributions of andesite have been commonly used to model volcanic ash (e.g. Wen and Rose, 1994; Pavolonis et al., 2006; Prata and Grant, 2001). The andesite particles were assumed to be spherical and Mie theory is used to compute the single scatter properties. Of course, real volcanic ash particles actually take on a variety of irregular shapes that are very difficult to model, and the ash composition (e.g. the type of rock) varies from volcano to volcano. Fortunately, the sensitivity to particle habit and composition in the infrared is much smaller than the sensitivity to particle size (Wen and Rose, 1994). Given the composition and habit assumptions, the needed β relationship can be computed from the Mie generated single scatter properties. Figure 6 below shows the variation of the 11 and 12 μm β with the 11 and 13.3 μm β computed using Equation 13, where the 11 μm channel is always placed in the denominator of Equation 13. Hereafter, these β's are referred to as β(12/11μm) and β(13.3/11μm), respectively. In the retrieval, β(12/11μm) is a free parameter and β(13.3/11μm) is determined using the empirical relationship shown in Figure 6. The form of the empirical relationship is as follows.

$$\beta(13.3/11\mu m) = c4[\beta(12/11\mu m)]^4 + c3[\beta(12/11\mu m)]^3 + c2[\beta(12/11\mu m)]^2 + c1[\beta(12/11\mu m)] + c0$$

(Eq. 15)

The coefficients used in Equation 15 are listed as a function of sensor in Table 2.

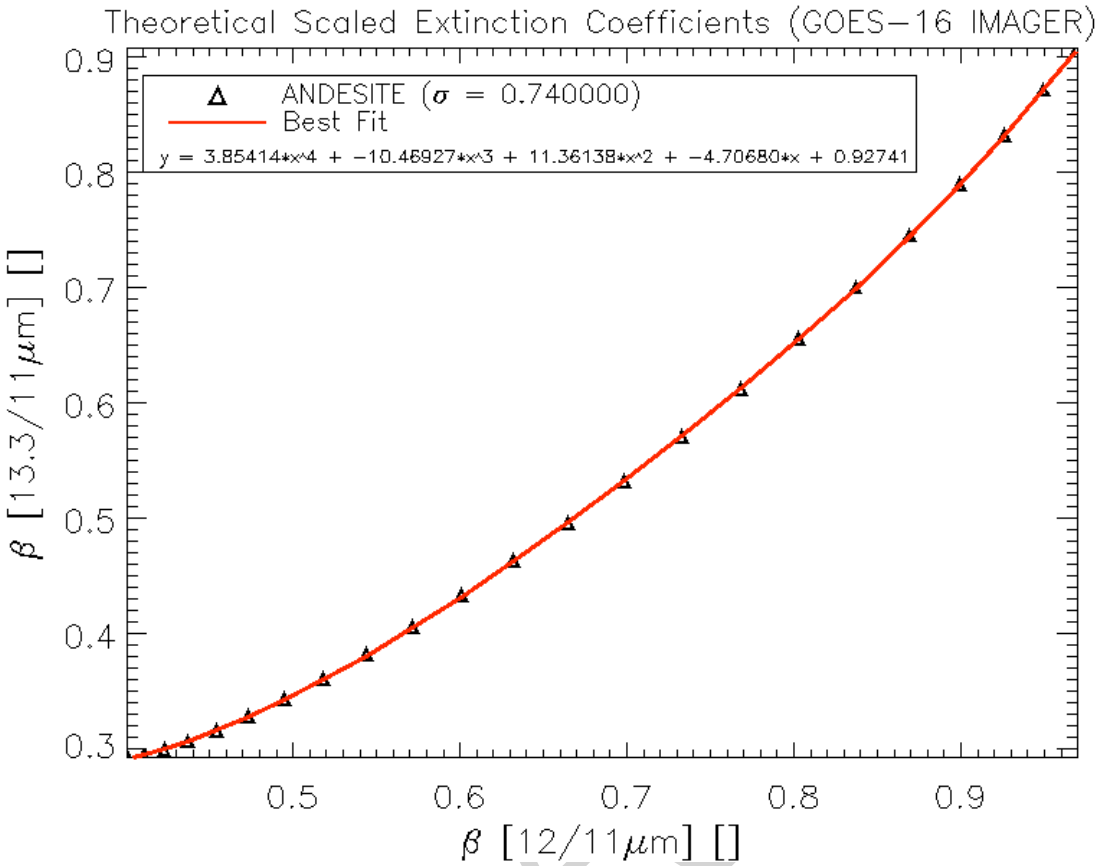

Figure 6: The 13.3/11 µm scaled extinction ratio (β(13.3/11 µm)) is shown as a function of the 12/11 µm scaled extinction ratio (β(12/11 µm)) for andesite spheres (volcanic ash). The andesite effective particle radius was varied from 1 to 13 µm, where larger values of β indicate larger particles. These β's were derived from single scatter properties calculated using Mie Theory and integrated over the corresponding ABI spectral response functions. The red line is the fourth degree polynomial fit.

Table 2: Regression coefficients needed to determine β(13.3/11µm) from β(12/11µm) using Equation 15. The coefficients are given as a function of sensor.

Sensor	C0	C1	C2	C3	C4
GOES-R ABI	0.92741	-4.70680	11.36138	-10.46927	3.85414
MET-8 SEVIRI	0.363415	-1.95058	6.22212	-6.67325	2.94788
MET-9 SEVIRI	0.307669	-1.57123	5.35150	-5.74824	2.57427
Terra MODIS	0.821825	-4.41789	11.0984	-10.8378	4.26339
Aqua MODIS	0.813096	-4.35587	10.9564	-10.6888	4.20431

Additional single scatter property based microphysical relationships are needed to convert the retrieved β(12/11μm) to an effective particle radius (r_{eff}) and the 11-μm extinction cross section ($\sigma_{ext}(11\mu m)$). Both of these parameters are needed when estimating the ash mass loading. Figure 7 and Figure 8 show the relationship used to convert the retrieved β(12/11μm) to an effective particle radius and extinction coefficient, respectively. The forms of these empirical relationships are as follows.

$$r_{eff} = \exp(c4[\beta(12/11\mu m)]^4 + c3[\beta(12/11\mu m)]^3 + c2[\beta(12/11\mu m)]^2 + c1[\beta(12/11\mu m)] + c0)$$

(Eq. 16)

$$\sigma_{ext}(11\mu m) = \exp(c4[\beta(12/11\mu m)]^4 + c3[\beta(12/11\mu m)]^3 + c2[\beta(12/11\mu m)]^2 + c1[\beta(12/11\mu m)] + c0)$$

(Eq. 17)

For notational convenience, generic symbols are used for the regression coefficients, which actually differ between Equations 15 - 17. The regression coefficients used in these expressions are given in Table 3 and Table 4 as a function of sensor.

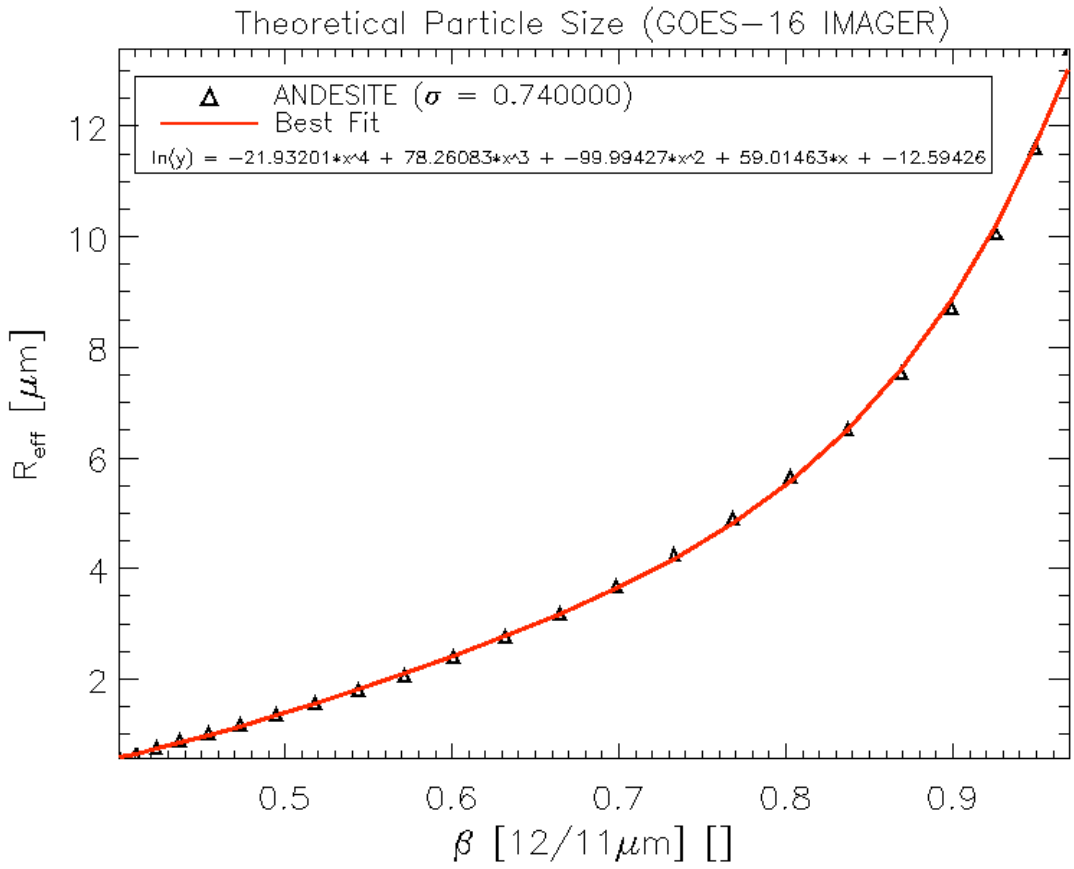

Figure 7: The effective particle radius is shown as a function of the 12/11 μm scaled extinction ratio (β(12/11 μm)) for andesite spheres (volcanic ash). The β(12/11 μm) was derived from single scatter properties calculated using Mie Theory and

integrated over the corresponding ABI spectral response functions. The red line is the fourth degree polynomial fit.

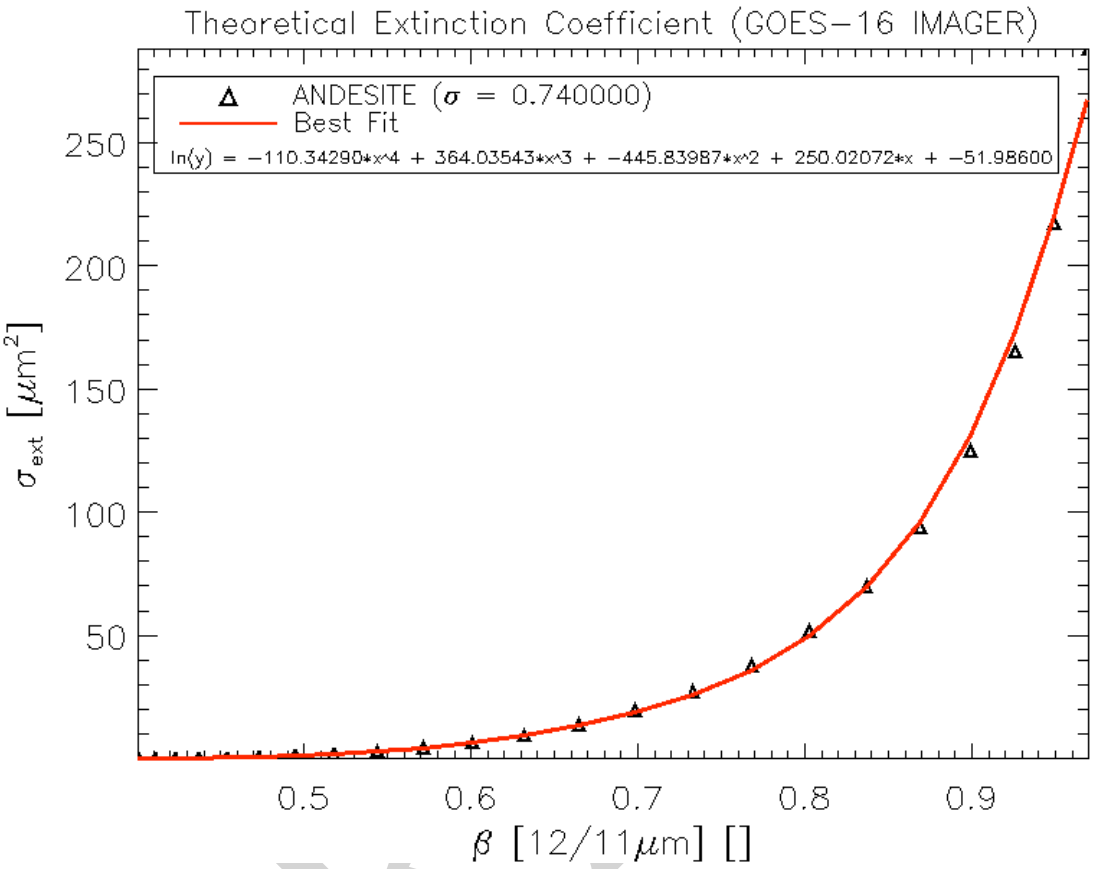

Figure 8: The extinction cross section is shown as a function of the 12/11 μm scaled extinction ratio (β(12/11 μm)) for andesite spheres (volcanic ash). The β(12/11 μm) was derived from single scatter properties calculated using Mie Theory and integrated over the corresponding ABI spectral response functions. The red line is the fourth degree polynomial fit.

Table 3: Regression coefficients needed to determine the effective particle radius in μm from β(12/11μm) using Equation 16. The coefficients are given as a function of sensor.

Sensor	C0	C1	C2	C3	C4
GOES-R ABI	-12.5943	59.0146	-99.9943	78.2608	-21.9320
MET-8 SEVIRI	-3.22925	10.6954	-5.17920	-5.68616	5.93906
MET-9 SEVIRI	-3.25818	11.8129	-8.69544	-1.56236	4.25769
Terra MODIS	-7.52014	30.9347	-42.0031	24.8926	-3.66602

Aqua MODIS	-7.52817	31.0711	-42.4260	25.4010	-3.87514

Table 4: Regression coefficients needed to determine the 11-μm extinction cross section in μm^2 from β(12/11μm) using Equation 17. The coefficients are given as a function of sensor.

Sensor	C0	C1	C2	C3	C4
GOES-R ABI	-51.9860	250.021	-445.840	364.035	-110.343
MET-8 SEVIRI	-13.2727	50.7207	-57.8280	25.4477	0.468358
MET-9 SEVIRI	-13.0247	52.3100	-64.7302	34.1704	-3.16255
Terra MODIS	-32.1321	141.961	-226.231	165.702	-43.5852
Aqua MODIS	-32.1062	142.052	-226.784	166.517	-43.9565

3.4.4 Mathematical Description

The mathematical approach employed here is the optimal estimation approach described by Rodgers (1976). The optimal estimation approach is also often referred to as a 1DVAR approach. The benefits of this approach are that it is flexible and allows for the easy addition or subtraction of new observations or retrieved parameters. Another benefit of this approach is that it generates automatic estimates of the retrieval errors. The optimal estimation approach minimizes a cost function, ϕ, given by

$$\phi = (x - x_a)^T S_a^{-1}(x - x_a) + (y - f(x))^T S_y^{-1}(y - f(x)) \quad \text{(Eq. 18)}$$

Where y is the vector of observations, x is the vector of retrieved parameters, f(x) represents the forward model, which is a function of x, and x_a is the *a priori* value of x. The matrices S_y and S_a are the error covariance matrices of the forward model and *a priori* values respectively. In our retrieval, the y, x, and x_a vectors are defined as follows.

$$y = \begin{pmatrix} BT(11\mu m) \\ BTD(11-12\mu m) \\ BTD(11-13.3\mu m) \end{pmatrix} \quad \text{(Eq. 19a)} \qquad x = \begin{pmatrix} T_{eff} \\ \varepsilon(11\mu m) \\ \beta(12/11\mu m) \end{pmatrix} \quad \text{(Eq. 19b)}$$

$$x_a = \begin{pmatrix} T_{eff}\_ap \\ \varepsilon(11\mu m)\_ap \\ \beta(12/11\mu m)\_ap \end{pmatrix} \quad \text{(Eq. 19c)}$$

The observation vector, y, consists of the 11 μm (ABI Channel 14) brightness temperature (BT), the 11 minus 12 μm (ABI Channel 14 – Channel 15) brightness temperature difference (BTD) and the 11 – 13.3 μm (ABI Channel 14 – Channel 16) BTD. The use of BTD's is needed to capture the cloud microphysical signal. The retrieved parameters, x, are the effective cloud temperature (T_{eff}), the 11 μm cloud emissivity (ε(11μm)), and the 12/11 μm effective absorption optical depth ratio (β(12/11μm)). The symbols for the first guess or *a priori* estimates of the retrieved parameters are appended with "_ap." As explained earlier, these retrieved parameters are then used to estimate the ash cloud height and mass loading. The ash height and mass loading cannot be retrieved directly because they are not variables in the cloudy infrared radiative transfer equation.

3.4.4.1 Determining the *a priori* Values and Associated Uncertainty

The *a priori* values and their associated uncertainties act to constrain the retrieved parameters when the measurements contain little or no information on one or more of the retrieved parameters. The *a priori* error covariance matrix (Equation 20) is assumed to be diagonal (e.g. errors in the first guess of each parameter are uncorrelated). The *a priori* values and their uncertainties depend on whether the ash cloud overlaps a lower meteorological cloud or if it is single layered, as determined by the volcanic ash detection routine. Table 5 shows the *a priori* values and their estimated uncertainties for both single and multilayered conditions. When forming the matrix given by Equation 20, the values in Table 5 need to be squared. These values were largely determined through analysis of semi-transparent ice clouds observed by spaceborne lidar (e.g. Heidinger and Pavolonis, 2009). Thus, these *a priori* estimates may not be ideal for volcanic ash clouds, but lidar observations of ash clouds are very rare, so better estimates are difficult to make. A large uncertainty is assigned to each *a priori* parameter, so that the measurements are given a high weight during the iteration. In summary, these values will likely be adjusted as more unique observations (e.g. lidar, in-situ, etc…) of volcanic ash clouds become available.

$$S_a = \begin{pmatrix} \sigma^2_{Teff\_ap} & 0.0 & 0.0 \\ 0.0 & \sigma^2_{\varepsilon(11\mu m)\_ap} & 0.0 \\ 0.0 & 0.0 & \sigma^2_{\beta(12/11\mu m)\_ap} \end{pmatrix} \quad \text{(Eq. 20)}$$

Table 5: The *a priori* (first guess) retrieval values used in the ABI volcanic ash retrieval. The T_{eff} first guess is a function of the 11 μm brightness temperature, B(11μm). The ε(11μm) first guess is a function of the satellite zenith angle, θ_{sat}.

Parameter	Single Layer *a priori*	Single Layer *a priori* Uncertainty	Multi-layer *a priori*	Multi-layer *a priori* Uncertainty
σ_{Teff_ap}	BT(11μm) – 15 K	50 K	BT(11μm) – 15 K	50 K

$\sigma_{\varepsilon(11\mu m)\_ap}$	$1.0\text{-}e^{(-0.5/\cos(\theta sat))}$	0.9	$1.0\text{-}e^{(-0.5/\cos(\theta sat))}$	0.9
$\sigma_{\beta(12/11\mu m)\_ap}$	0.5	0.4	0.5	0.4

3.4.4.2 The Forward Model

For notational convenience, we define the "blackbody" top-of-atmosphere cloud radiance, $R_{cld}(\lambda)$, as follows. All other terms in this equation have been defined previously.

$$R_{cld}(\lambda) = R_{ac}(\lambda) + t_{ac}(\lambda)B(\lambda, T_{eff}) \quad \text{(Eq. 21)}$$

Based on Equations 10 and 21, the radiance for each channel used in the retrieval is given by Equations 22 – 24. The Planck Function is then used to convert the radiances to brightness temperature, from which brightness temperature differences can be constructed.

$$R_{obs}(11\mu m) = \varepsilon(11\mu m)R_{cld}(11\mu m) + R_{clr}(11\mu m)(1 - \varepsilon(11\mu m)) \quad \text{(Eq. 22)}$$

$$R_{obs}(12\mu m) = \varepsilon(12\mu m)R_{cld}(12\mu m) + R_{clr}(12\mu m)(1 - \varepsilon(12\mu m)) \quad \text{(Eq. 23)}$$

$$R_{obs}(13.3\mu m) = \varepsilon(13.3\mu m)R_{cld}(13.3\mu m) + R_{clr}(13.3\mu m)(1 - \varepsilon(13.3\mu m)) \quad \text{(Eq. 24)}$$

The 12 and 13.3 μm cloud emissivities are not retrieved, so they must be determined at the beginning of each iteration in the optimal estimation scheme using ε(11μm), β(12/11μm), and Equation 15 (in the case of ε(13.3μm)) to evaluate the following relationships, which were derived from Equation 12.

$$\varepsilon(12\mu m) = 1 - [1 - \varepsilon(11\mu m)]^{\beta(12/11\mu m)} \quad \text{(Eq. 25)}$$

$$\varepsilon(13.3\mu m) = 1 - [1 - \varepsilon(11\mu m)]^{\beta(13.3/11\mu m)} \quad \text{(Eq. 26)}$$

If the volcanic ash detection results indicate that an ash cloud likely overlaps a lower meteorological cloud, then the clear sky radiance, $R_{clr}(\lambda)$, in Equations 22 – 24 is replaced by the radiance from and above a black (emissivity = 1 at all wavelengths) elevated surface in an effort to account for the impact of the lower cloud layer. The mechanism used to compute the top-of-atmosphere radiance from and above the elevated black surface is described in detail in Section 3.4.2.1.

The errors associated with the forward model, f(x), must be characterized and expressed in the forward model error covariance matrix, S_y (Equation 27). The largest source of uncertainty in the forward model is the clear sky radiative transfer. The uncertainty in the clear sky radiative transfer should include the effects of errors in the surface temperature, surface emissivity, and atmospheric profiles. Spatial heterogeneity is another source of error since the retrieval assumes that each pixel is uniformly cloudy. Instrumental issues, such as those due to calibration and noise effects, also contribute to the forward model

error. Thus, the total uncertainty in the forward model is assumed to be composed of a linear combination of three major sources (see Equation 28): instrumental, clear sky radiative transfer modeling, and pixel heterogeneity. In Equation 28, the instrument uncertainty is given by σ^2_{instr}, the clear sky radiative transfer uncertainty is denoted by σ^2_{clr}, and the uncertainty due to pixel heterogeneity is given by σ^2_{hetero}. The impact of the clear sky radiative transfer uncertainty is approximately inversely proportional to the cloud emissivity, so it is weighted by the 11-μm cloud emissivity, ε(11μm). The off-diagonal elements (correlated uncertainty) of the forward model error covariance matrix are very difficult to determine, so only the diagonal elements (uncorrelated uncertainty) are considered.

$$S_y = \begin{pmatrix} \sigma^2_{BT(11\,\mu m)} & 0.0 & 0.0 \\ 0.0 & \sigma^2_{BTD(11\,-\,12\,\mu m)} & 0.0 \\ 0.0 & 0.0 & \sigma^2_{BTD(11\,-\,13.3\,\mu m)} \end{pmatrix} \quad \text{(Eq. 27)}$$

$$\sigma^2 = \sigma^2_{instr} + [1 - \varepsilon(11\mu m)]\sigma^2_{clr} + \sigma^2_{hetero} \quad \text{(Eq. 28)}$$

The uncertainty in the clear sky radiative transfer (σ^2_{clr}) is determined through a radiance bias analysis. The radiance bias estimates should be monitored over time and changes to σ^2_{clr} should be made accordingly. The current estimates of σ^2_{clr}, which are shown in Table 6, are based on analysis of Spinning Enhanced Visible and Infrared Imager (SEVIRI) data. These estimates will need to be updated during the early orbit period of the ABI as explained in detail in the ABI Volcanic Ash Product Validation Plan document. As expected, the uncertainty over land surfaces is larger than over open water. Over land, larger errors in surface temperature and surface emissivity results in larger radiance biases compared to water surfaces. It should be noted that the clear sky radiance biases will become smaller as clear sky radiative transfer models, numerical weather prediction models, and surface emissivity estimates improve.

The forward model uncertainty due to spatial heterogeneity (σ^2_{hetero}) is approximated by the variance of each observation used in the retrieval over a 3 x 3 pixel box centered on the current pixel of interest. The last and probably least significant forward model error term is that due to instrumental effects, σ^2_{instr}. This term includes noise, calibration, and spectral response errors. The current conservative estimates of this uncertainty are given in Table 6. Similar to the uncertainty estimates associated with the clear sky radiative transfer, these will need to be updated during the early orbit period.

Table 6: The individual components of the total forward model uncertainty used in the ABI volcanic ash retrieval. The total uncertainty is given by Equation 28. These values need to be squared when building the matrix given by Equation 27.

Parameter	Instrument Uncertainty (σ_{instr})	Clear Sky Radiance Uncertainty (σ_{clr}) (Land, Water)	Non-uniform Pixel Uncertainty (σ_{hetero})
$\sigma_{BT(11\mu m)}$	1.0 K	5.0 K, 1.5 K	variable (see text)

$\sigma_{BTD(11\text{-}12\mu m)}$	1.0 K	1.0 K, 0.5 K	variable (see text)
$\sigma_{BTD(11\text{-}13.3\mu m)}$	2.0 K	4.0 K, 2.0 K	variable (see text)

3.4.4.3 Optimal Estimation Iterations

Each step in the optimal estimation iteration changes each element of x as governed by the following relationship

$$\delta x = S_x K^T S_y^{-1}[y - f(x)] + S_a^{-1}(x_a - x) \quad \text{(Eq. 29)}$$

where δx is the increment in x and S_x is error covariance matrix of x and K is the Kernel or Jacobian matrix. The Kernel matrix contains the partial derivatives of each element of f to each element of x as follows.

$$K = \begin{pmatrix} \frac{\partial BT(11\mu m)}{\partial T_{eff}} & \frac{\partial BT(11\mu m)}{\partial \varepsilon(11\mu m)} & \frac{\partial BT(11\mu m)}{\partial \beta(12/11\mu m)} \\ \frac{\partial BTD(11-12\mu m)}{\partial T_{eff}} & \frac{\partial BTD(11-12\mu m)}{\partial \varepsilon(11\mu m)} & \frac{\partial BTD(11-12\mu m)}{\partial \beta(12/11\mu m)} \\ \frac{\partial BTD(11-13.3\mu m)}{\partial T_{eff}} & \frac{\partial BTD(11-13.3\mu m)}{\partial \varepsilon(11\mu m)} & \frac{\partial BTD(11-13.3\mu m)}{\partial \beta(12/11\mu m)} \end{pmatrix} \quad \text{(Eq. 30)}$$

Given our choice of forward model, an analytical expression for each element of K can be derived from Equations 22 – 26, Equation 15, and the Planck Function. The derivative of each of the forward model simulated observations with respect to T_{eff} is given by the following set of equations. In these equations, ∂B(λ)/∂T is the derivative of the Planck Function with respect to temperature. All other symbols have been previously defined.

$$\frac{\partial BT(11\mu m)}{\partial T_{eff}} = \varepsilon(11\mu m) t_{ac}(11\mu m) \left(\frac{\partial B(11\mu m)}{\partial T_{eff}}\right)\left(\frac{\partial B(11\mu m)}{\partial T}\right)^{-1} \quad \text{(Eq. 31)}$$

$$\frac{\partial BTD(11-12\mu m)}{\partial T_{eff}} = \frac{\partial BT(11\mu m)}{\partial T_{eff}} - \varepsilon(12\mu m) t_{ac}(12\mu m) \left(\frac{\partial B(12\mu m)}{\partial T_{eff}}\right)\left(\frac{\partial B(12\mu m)}{\partial T}\right)^{-1} \quad \text{(Eq. 32)}$$

$$\frac{\partial BTD(11-13.3\mu m)}{\partial T_{eff}} = \frac{\partial BT(11\mu m)}{\partial T_{eff}} - \varepsilon(13.3\mu m) t_{ac}(13.3\mu m) \left(\frac{\partial B(13.3\mu m)}{\partial T_{eff}}\right)\left(\frac{\partial B(13.3\mu m)}{\partial T}\right)^{-1} \quad \text{(Eq. 33)}$$

The following equations give the derivative of each forward model simulation with respect to ε(11μm).

$$\frac{\partial BT(11\mu m)}{\partial \varepsilon(11\mu m)} = [R_{cld}(11\mu m) - R_{clr}(11\mu m)]\left(\frac{\partial B(11\mu m)}{\partial T}\right)^{-1} \quad \text{(Eq. 34)}$$

$$\frac{\partial BTD(11-12\mu m)}{\partial \varepsilon(11\mu m)} =$$

$$\frac{\partial BT(11\mu m)}{\partial \varepsilon(11\mu m)} - [R_{cld}(12\mu m) - R_{clr}(12\mu m)][\beta(12/11\mu m)(1-\varepsilon(11\mu m))^{\beta(12/11\mu m)-1}]\left(\frac{\partial B(12\mu m)}{\partial T}\right)^{-1}$$

(Eq. 35)

$$\frac{\partial BTD(11-13.3\mu m)}{\partial \varepsilon(11\mu m)} =$$

$$\frac{\partial BT(11\mu m)}{\partial \varepsilon(11\mu m)} - [R_{cld}(13.3\mu m) - R_{clr}(13.3\mu m)][\beta(13.3/11\mu m)(1-\varepsilon(11\mu m))^{\beta(13.3/11\mu m)-1}]\left(\frac{\partial B(13.3\mu m)}{\partial T}\right)^{-1}$$

(Eq. 36)

Finally, the derivative of each forward model simulation with respect to β(12/11μm) is given by the following equations. In Equation 39, ∂β(13.3/11μm)/∂β(12/11μm) is applied to Equation 15.

$$\frac{\partial BT(11\mu m)}{\partial \beta(12/11\mu m)} = 0.0 \quad \text{(Eq. 37)}$$

$$\frac{\partial BTD(11-12\mu m)}{\partial \beta(12/11\mu m)} = [R_{cld}(12\mu m) - R_{clr}(12\mu m)]\ln[1-\varepsilon(11\mu m)][1-\varepsilon(12\mu m)]\left(\frac{\partial B(12\mu m)}{\partial T}\right)^{-1}$$

(Eq. 38)

$$\frac{\partial BTD(11-13.3\mu m)}{\partial \beta(12/11\mu m)} =$$

$$[R_{cld}(13.3\mu m) - R_{clr}(13.3\mu m)]\ln[1-\varepsilon(11\mu m)][1-\varepsilon(13.3\mu m)]\left(\frac{\partial \beta(13.3/11\mu m)}{\partial \beta(12/11\mu m)}\right)\left(\frac{\partial B(13.3\mu m)}{\partial T}\right)^{-1}$$

(Eq. 39)

Once the Kernel Matrix has been calculated, the error covariance matrix of x (Equation 40) can be determined using Equation 41 (Rodgers, 1976).

$$S_x = \begin{pmatrix} \sigma^2_{Teff} & 0.0 & 0.0 \\ 0.0 & \sigma^2_{\varepsilon(11\mu m)} & 0.0 \\ 0.0 & 0.0 & \sigma^2_{\beta(12/11\mu m)} \end{pmatrix} \quad \text{(Eq. 40)}$$

$$S_x = (S_a^{-1} + K^T S_y^{-1} K)^{-1} \quad \text{(Eq. 41)}$$

The optimal estimation approach is run until the following convergence criterion is met.

$$\left\| \sum \delta x S_x^{-1} \delta x \right\| \leq \frac{p}{2} \quad \text{(Eq. 42)}$$

Where p is the size of x, which is 3 in our case. This convergence criterion is taken out of Rodgers (1976). If the retrieval does not converge after 10 iterations, it is deemed a failed retrieval. In the event of a failed retrieval, all retrieved parameters are set to missing, not the *a priori* values. The *a priori* values are not used since ash cloud properties are highly variable in time and space and cannot be accurately parameterized by guess values alone. Very few retrievals (< 0.01%) fail to converge, so this has a negligible impact on the ash products. Further, δx is constrained such that the maximum allowed absolute changes in the retrieved parameters, T_{eff}, ε(11μm), and β(12/11μm), are 20.0 K, 0.2, 0.2, respectively. Once the retrieval vector is updated by δx, the retrieved parameters are constrained to be within a certain physically based range. Table 7 shows the allowed min and max values of each retrieved parameter.

Table 7: The valid range for each retrieved parameter.

Parameter	Minimum Allowed Value	Maximum Allowed Value
T_{eff}	160 K	NWP surface temperature
ε(11μm)	0.0	1.0
β(12/11μm)	0.20	1.05

3.4.4.4 Retrieval Quality Flags

The actual retrieval error estimates are given by the square root of the diagonal elements of S_x. The information from these error estimates is packed into a quality flag for each parameter by comparing the error in the retrievals to the uncertainty of the *a priori* estimates using the following logic.

Quality is judged based on how much the first guess is improved (or not). The highest quality is assigned to a given retrieved parameter when $S_x(n,n) < 0.111*S_a(n,n)$, where n is the index of the retrieved parameter. Intermediate quality is assigned to a given retrieved parameter when $0.111*S_a(n,n) \leq S_x(n,n) < 0.444*S_a(n,n)$. The lowest quality is assigned when $S_x(n,n) \geq 0.444*S_a(n,n)$. The factors 0.111 and 0.444 correspond to the square root of 1/3 and 2/3, respectively.

3.4.4.5 Computation of Cloud Height

The retrieved T_{eff} is used to estimate the ash cloud height. First, linear interpolation weights and anchor points are determined by locating T_{eff} within the NWP temperature profile. The temperature profile is searched from high to low vertical levels. The weights and anchor points are then used to determine the ash cloud height. Equation 43 illustrates the interpolation technique. In Equation 43, Z_{ash} is the ash cloud height. T1 and T2 are the temperatures within the profile that bound T_{eff}, with T1 being the temperature at the highest (e.g. furthest from the ground) bounding level. Z1 and Z2 are the corresponding height of the bounding temperatures, T1 and T2.

$$Z_{ash} = Z1 + \left(\frac{T_{eff} - T1}{T2 - T1}\right)(Z2 - Z1) \quad \text{(Eq. 43)}$$

3.4.4.6 Computation of Ash Mass Loading

The method for computing ash mass loading is based on the methodology used by Zhang et al. (2006). The ash mass loading is computed from the retrieved 11-μm cloud emissivity (ε(11μm)) and the retrieved β(12/11 μm). First, the effective 11-μm emissivity is converted to an effective optical depth, τ(11μm), using:

$$\tau(11\mu m) = -\cos(\theta_{sat})\ln[1.0 - \varepsilon(11\mu m)] \quad \text{(Eq. 44)}$$

In Equation 44, θ_{sat} is the satellite zenith angle. Next, the retrieved β(12/11 μm) is used to determine the effective particle radius (r_{eff}) and the 11-μm extinction cross-section ($\sigma_{ext}(11\mu m)$) by applying the regression relationships given by Equations 16 and 17.

As described in Section 3.4.3.2, the ash distribution is assumed to be lognormal. Lognormal distributions have the following form.

$$n(r) = \frac{N_o}{\sqrt{2\pi}}\frac{1}{r\ln\sigma}e^{\left[\frac{(\ln r - \ln r_{mod})^2}{2(\ln\sigma)^2}\right]} \quad \text{(Eq. 45)}$$

In Equation 45, n(r) is the number particles per unit area per bin of particle size. N_o is the total number of particles per unit area, r is the particle radius, r_{mod} is the modal radius, and σ is the width parameter of the lognormal distribution which is taken to be 0.74 (Wen and Rose, 1994). The modal radius, r_{mod} is calculated from the effective radius, r_{eff}.

$$r_{mod} = \frac{r_{eff}}{e^{\left[\frac{5}{2}(\ln\sigma)^2\right]}} \quad \text{(Eq. 46)}$$

The total number of particles per unit area is determined from the 11-μm cloud optical depth and the 11-μm extinction cross section using Equation 47.

$$N_o = \frac{\tau(11\mu m)}{\sigma_{ext}(11\mu m)} \quad \text{(Eq. 47)}$$

Finally, the mass loading is computed using:

$$ML = (1\times10^6)\frac{4}{3}\pi\rho_{ash}\int_{r_1}^{r_2} r^3 n(r)dr \quad \text{(Eq, 48)}$$

In Equation 48, ML is the mass loading in tons/km^2 and ρ_{ash} is the density of ash, which is taken to be 2.6 g/cm^3 (Neal et al., 1994). The particle radius, r, is expressed in units of

μm. The units of n(r) are the number of particles per μm^2 per μm. The factor, $1x10^6$, in Equation 48, is needed to convert the units to tons/km^2.

3.4.5 Algorithm Output

The ABI Volcanic Ash Algorithm produces the following products listed in the F&PS.

- Ash cloud height [km]
- Ash mass loading [tons/km^2]

The above products are derived at the pixel level for all pixels that potentially contain volcanic ash. For pixels that do not contain volcanic ash, the ash cloud height will be set to missing (-999.0) and the ash mass loading will be set to 0.0. When the ash retrieval fails, which is very rare, both the ash height and ash mass loading will be set to missing (-999.0). Example ash cloud height and ash mass loading output are shown in Figure 11.

In addition, the ABI Volcanic Ash Algorithm produces quality flags. The quality flags contain the following information for each pixel.

- ash detection confidence (3 bits)
- multilayered ash flag (1 bit)
- ash spatial uniformity flag (2 bits)
- T_{eff} retrieval quality (2 bits)
- ε(11μm) retrieval quality (2 bits)
- β(12/11μm) retrieval quality (2 bits)
- ash particle size (8 bits)

4 TEST DATA SETS AND OUTPUTS

4.1 Simulated/Proxy Input Data Sets

As described below, the data used to test the ABI Volcanic Ash Algorithm (ABI-VAA) consists of Spinning Enhanced Visible and Infrared Imager (SEVIRI) observations. SEVIRI has observed several volcanic ash clouds. Given its coverage of the Sahara Desert, SEVIRI also commonly observes dust clouds. Dust is spectrally similar to volcanic ash in the infrared (see Figure 2 and Figure 3), so it can also be used to test the ash algorithms. In addition, several ash and dust free scenes were processed as a way of assessing the false alarm rate of the ash detection algorithm. Moderate Resolution Imaging Spectrometer (MODIS) data will also be used as an ABI proxy at later stages of the algorithm development and validation process. The rest of this section describes the proxy and validation data sets used in assessing the performance of the ABI-VAA.

4.1.1 SEVIRI Data

SEVIRI provides 11 spectral channels with a spatial resolution of 3 km and provides spatial coverage of the full disk with a temporal resolution of 15 minutes. SEVIRI provides the best source of data currently for testing and developing the ABI-VAA. Figure 9, shown below, is a full-disk SEVIRI image from 12 UTC on November 24, 2006. SEVIRI data are readily available from the University of Wisconsin Space Science and Engineering Center (SSEC) Data Center.

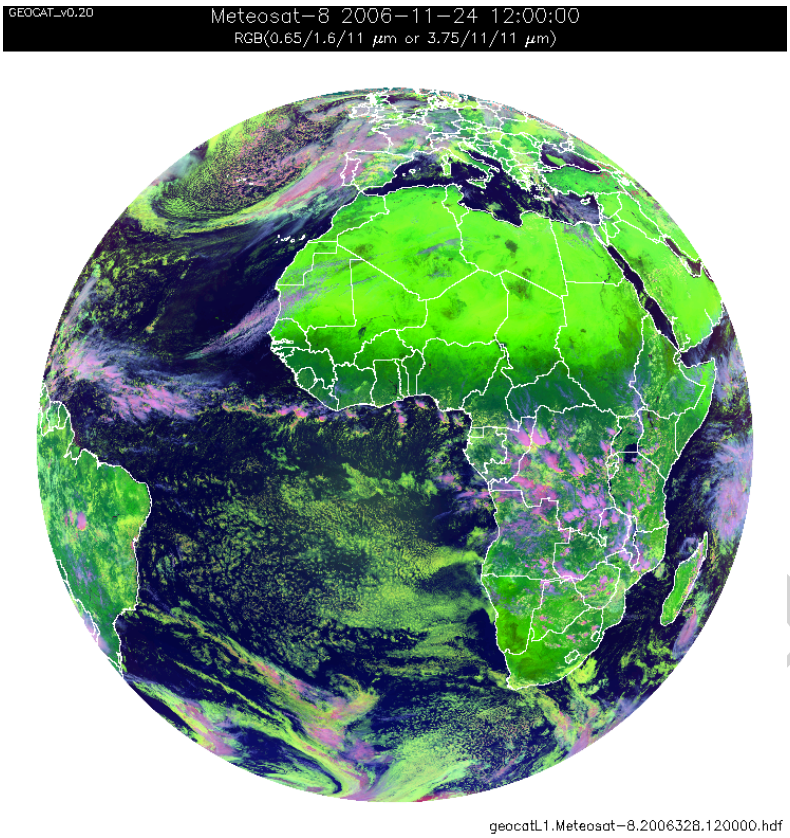

Figure 9: SEVIRI RGB image from 12 UTC on November 24, 2006.

4.1.1.1 CALIOP Data

With the launch of the Cloud-Aerosol Lidar and Infrared Pathfinder Satellite Observation (CALIPSO) into the EOS A-train in April 2006, the ability to validate satellite-based cloud and aerosol products increased significantly. The Cloud-Aerosol Lidar with Orthogonal Polarization (CALIOP) on-board the CALIPSO satellite is a dual wavelength depolarization lidar. We will primarily use the CALIOP cloud layer results to validate the volcanic ash height and mass loading products. The horizontal resolution of the CALIOP cloud layer data used in the validation is 1-km. An example 1-km CALIOP cross section is shown in Figure 10. All of the validation data sources and procedures, including CALIOP, are described in detail the ABI Volcanic Ash Product Validation Plan Document.

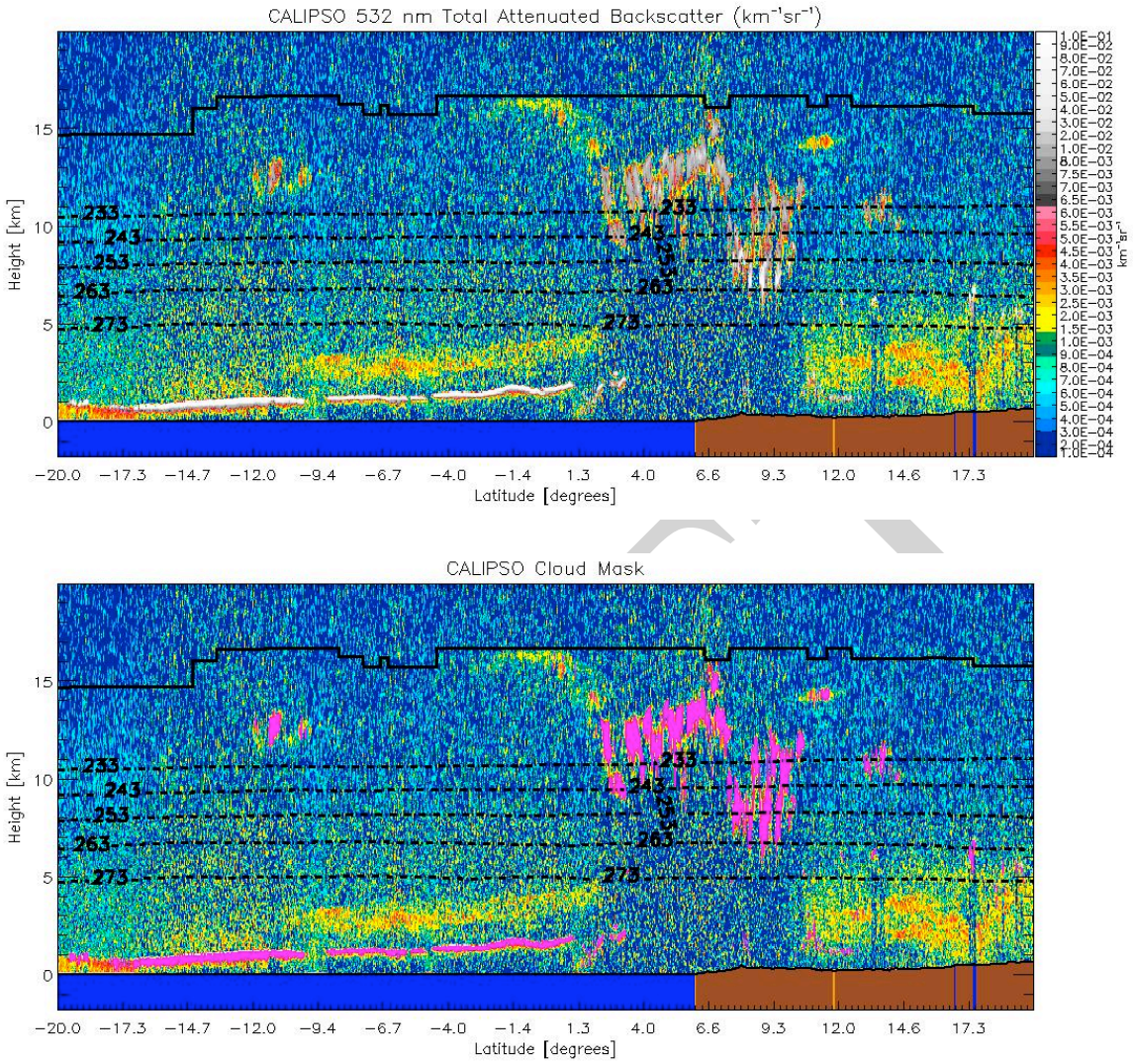

Figure 10: Illustration of the CALIOP data used in this study. Top image shows a 2d backscatter profile. Bottom image shows the detected cloud layers overlaid onto the backscatter image. Cloud layers are color magenta.

4.2 Output from Simulated/Proxy Inputs Data Sets

The ABI-VAA was tested on an eruption of Karthala captured by SEVIRI on November 24, 2005. Several other cases were processed, but only sample results from Karthala are shown below. Figure 11 shows the ABI ash height and the mass loading products. These images correspond to 12 UTC on November 24, 2005.

As shown at the Test Readiness Review (TRR), the ABI-VAA output from the online (Framework) and offline (Aviation AWG) processing systems match exactly. These tests

were conducted under different conditions using the same input for both the online and offline tests.

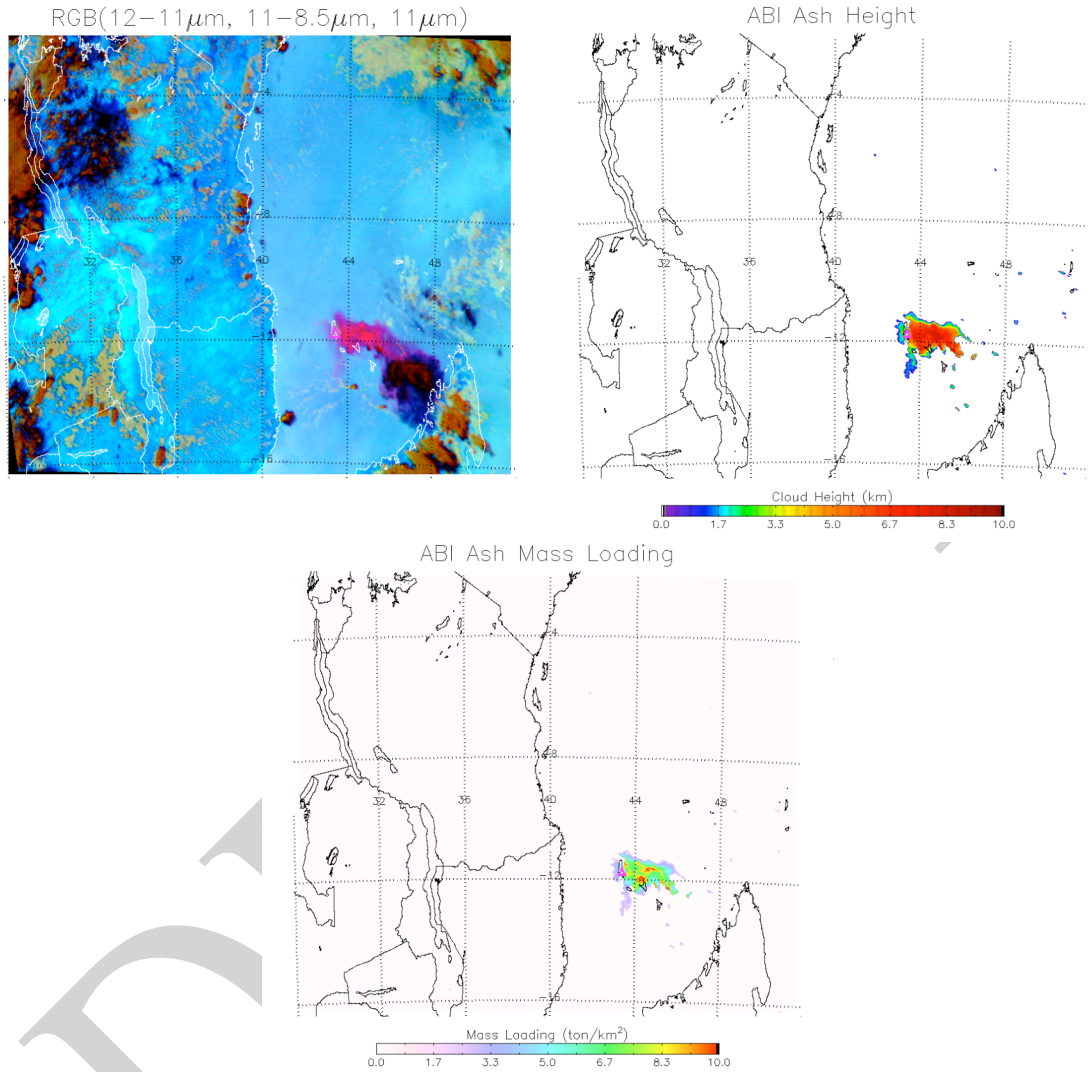

Figure 11: The ABI volcanic ash products were generated for an eruption of Karthala captured by SEVIRI. The volcanic ash cloud appears magenta in the false color image (top, left panel). The ash cloud height is shown in the top, right panel, and the ash mass loading is shown in the bottom panel.

4.2.1 Precisions and Accuracy Estimates

The GOES-R ABI volcanic ash requirements are expressed such that the vertical resolution is 3-km and the measurement accuracy and precision are 2.0 and 2.5 tons/km^2, respectively. The accuracy and precision thresholds obviously apply to the ash mass loading. We interpret the 3-km vertical resolution as the accuracy (bias) threshold for the volcanic ash cloud top height. Several different validation procedures are utilized.

Routine validation of the volcanic ash products is challenging given that volcanic ash clouds are rarely measured by active ground-based sensors or even by active spaceborne sensors such as the CALIOP. Targeted in-situ measurements do not exist since it is considered highly dangerous to fly manned aircraft into volcanic ash clouds. Our general validation plan is to supplement the infrequent spaceborne lidar observations of volcanic ash clouds with comparisons to ash products derived from instruments that are more sensitive to volcanic ash than the ABI. We will also employ vicarious validation techniques, where we apply the volcanic ash retrieval algorithm to other types of clouds that are commonly observed. Manual analysis can also be used to some extent.

Given the lack of direct measurements of volcanic ash clouds, truth is very difficult to define. Based on the validation that has been performed thus far, and the fact that this retrieval methodology has been applied successfully to meteorological clouds, the ABI volcanic ash products are expected to meet specification, relative to imperfect validation sources. The validation efforts are ongoing. Some early results are presented in the following section.

4.2.2 Error Budget

In the following sections, three different validation techniques (null validation, vicarious validation, and direct validation) are applied to the GOES-R volcanic ash products.

4.2.2.1 Validation of the Null Case

In the absence of a volcanic ash cloud, the retrieved ash mass loading should be 0 tons/km^2. This is referred to as the null case. *A posteriori* it well known which SEVIRI full disks are void of volcanic ash clouds, based on eruption records. Thus, a random sampling of SEVIRI full disks without volcanic ash can be chosen to quantify the retrieval error under these conditions. For a perfect algorithm, the bias (accuracy) distribution would be characterized by a delta function positioned at 0 tons/km^2 and the precision would be 0 tons/km^2. This sort of validation is important since a low ash detection false alarm rate is critical to users. Figure 12 shows the ash mass loading results from 8 SEVIRI full disks that did not contain ash or dust clouds (manual analysis was used to confirm the absence of dust clouds). Each full disk contains 1x10^7 pixels. The mean accuracy and precision (using 0.0 tons/km^2 as truth) are 0.015 tons/km^2 and 0.472 tons/km^2, respectively. The accuracy and precision for each of the 8 SEVIRI full disks are shown in Table 8. All of these values are well within the mass loading accuracy and precision specifications.

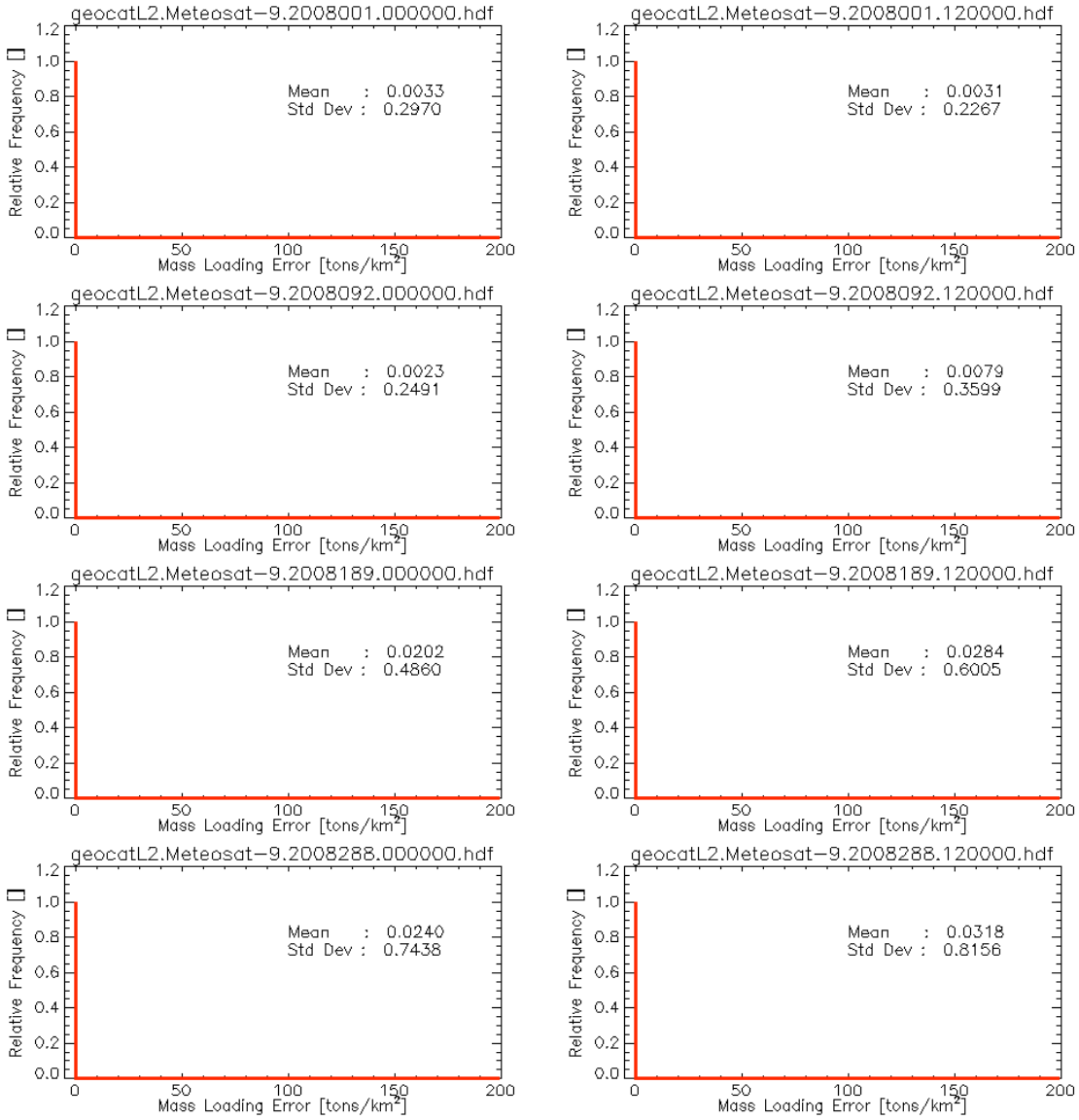

Figure 12: The retrieved ash mass loading for 8 different SEVIRI full disk scenes that were void of ash and dust clouds (the null case). Results for winter, spring, summer, and fall (00 and 12 UTC) are shown in the first, second, third, and fourth rows, respectively. In this null case, the correct answer is 0.0 tons/km^2. Thus, the mean represents the accuracy and the standard deviation represents the precision.

Table 8: The accuracy and precision of the ash mass loading product when applied to 8 SEVIRI full disks that were void of volcanic ash and dust. In this null case, the truth value is 0.0 tons/km^2.

Scene	Accuracy (tons/km^2)	Precision (tons/km^2)
January 1, 2008, 00 UTC	0.0033	0.2970
January 1, 2008, 12 UTC	0.0031	0.2267
April 1, 2008, 00 UTC	0.0023	0.2491

April 1, 2008, 12 UTC	0.0079	0.3599
July 7, 2008, 00 UTC	0.0202	0.4860
July 7, 2008, 12 UTC	0.0284	0.6005
October 14, 2008, 00 UTC	0.0240	0.7438
October 14, 2008, 12 UTC	0.0318	0.8156
Mean	0.0151	0.4723

4.2.2.2 Vicarious Validation

The volcanic ash retrieval described in this ATBD can be applied to meteorological clouds using modified cloud microphysical assumptions. CALIOP observations of meteorological clouds are very common, so a statistically significant validation analysis of meteorological clouds is possible. As shown in the ABI Cloud Height ATBD, the meteorological cloud height accuracy is well within the 3 km ash cloud specification, which gives confidence that the ash cloud heights will also be within the specification.

While the meteorological cloud analysis adds confidence, it is limited by the fact that volcanic ash clouds exhibit a very different spectral signature in the infrared. Applying the GOES-R ash retrieval to dust clouds can largely negate this limitation. Dust clouds, which are frequently observed by CALIOP, have a very similar spectral signature as ash clouds in the infrared (stronger absorption near 11 μm than at 12 and 13.3 μm). The GOES-R ash retrieval algorithm was applied to an elevated dust cloud layer observed by CALIOP on June 22, 2007 around 1515 UTC. It is straightforward to compare the cloud height retrieved by the GOES-R algorithm and the CALIOP-derived cloud top height, as is shown in Figure 13. The GOES-R heights fall within the dust cloud layer as depicted by the CALIOP 532 nm total attenuated backscatter. As expected, the GOES-R heights are biased low (Bias = -1.245 km, see Table 9) relative to the top boundary of the dust layer since the infrared measurements are sensitive to an extinction-weighted cloud temperature, not the cloud top temperature.

The mass loading product can also be validated using CALIOP. The CALIOP vertical cloud boundary information along with a co-located temperature profile (from NWP) can be used to determine a high quality effective cloud temperature estimate. Given the effective cloud temperature and estimates of the clear sky radiance, a "truth" cloud emissivity can be calculated for a give spectral channel. The "truth" 11-μm cloud emissivity and the "truth" β(12/11μm) can then be used to compute the mass loading using the procedure described in Sections 3.4.3.2 and 3.4.4.6. The major weakness of this procedure is that the microphysical assumptions used in converting the 11-μm cloud emissivity and the β(12/11μm) to mass loading cannot be validated. These assumptions can only be validated using in-situ measurements of ash clouds, which do not exist at this point. Table 9 shows that the retrieved mass loading agrees well with the mass loading calculated using the CALIOP vertical cloud boundaries. The accuracy and precision are 0.270 tons/km^2 and 0.269 tons/km^2, respectively. Both are well within the F&PS specifications. Since the sample size used in this analysis is small, additional comparisons to dust clouds will be performed. Also, the next version of the algorithm

will contain a quality flag, which will indicate the likelihood of dust versus ash based on spatial metrics.

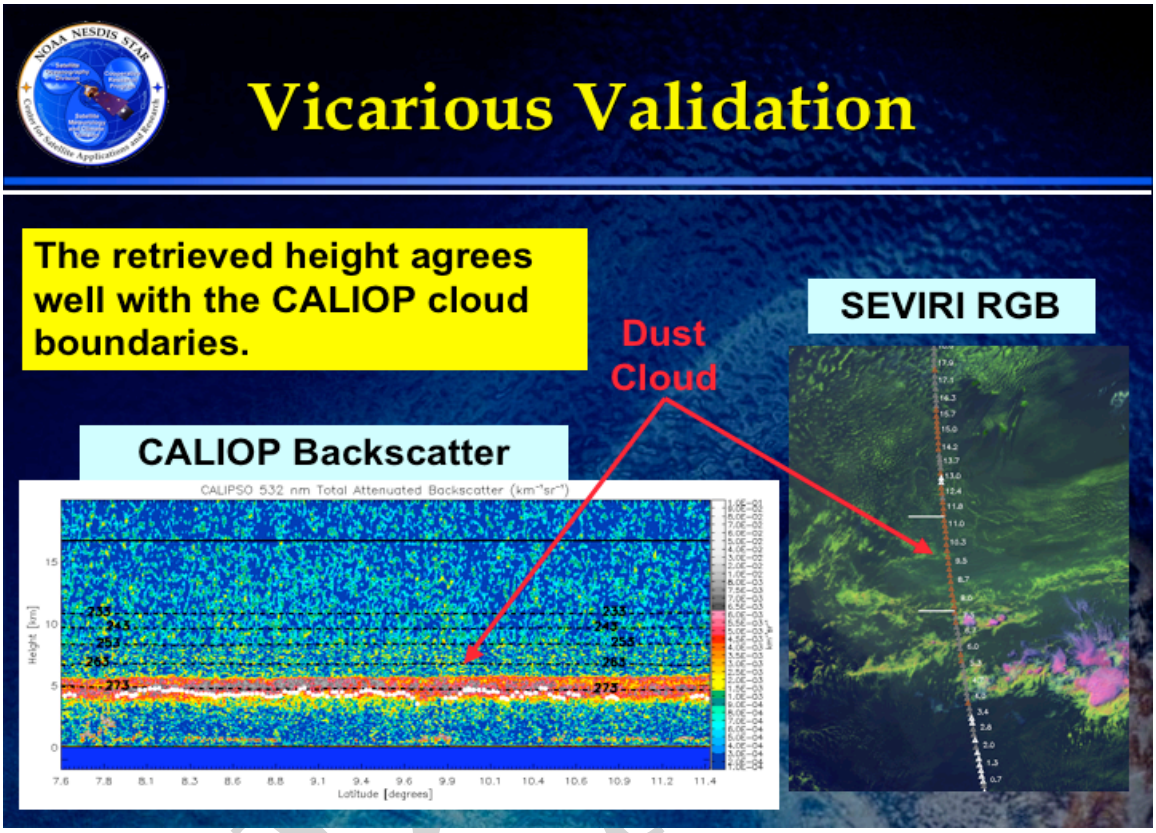

Figure 13: The GOES-R volcanic ash retrieval algorithm was applied to an elevated Saharan dust cloud, which exhibits a spectral signature that is very similar to ash in the infrared. The results of the height retrieval algorithm are overlaid (white circles) on a 532 nm CALIOP total attenuated backscatter cross section. The retrieval results agree well with the lidar positioning of the dust cloud.

Product	Accuracy (mean bias)	Precision (stddev of bias)
Ash Top Height	-1.245 km	0.464 km
Ash Mass Loading	0.270 tons/km^2	0.269 tons/km^2

Table 9: Accuracy (mean bias) and precision (standard deviation of bias) statistics derived from comparisons between CALIOP derived dust cloud top heights and mass loading and those retrieved using the GOES-R volcanic ash algorithm for 112 match-ups.

4.2.2.3 CALIOP Observations of Ash Clouds

CALIOP observations of ash clouds are quite rare, especially in the SEVIRI domain, but CALIOP and SEVIRI did sample the ash cloud produced by an eruption of Chaiten

(Chile) as it drifted across the South Atlantic Ocean in early May 2008. The ash observed by CALIOP on May 5, 2008 at 15:15 UTC was embedded in a very complicated vertical cloud distribution. As shown in Figure 14, the ash was distributed into two separate layers, both of which overlapped a lower layer of liquid water. The features labeled in Figure 14, were confirmed by examining the lidar depolarization ratio, which is large for a distribution of highly non-spherical volcanic ash particles compared to nearly spherical liquid water droplets. To further complicate matters, an optically thin ice cloud was present for a portion of the segment. The thin cirrus cloud prevents a valid retrieval from being performed in that part of the segment. Otherwise the ash cloud height retrieval produces a result that lies well within the layer bounded by the top of the highest ash layer and the bottom of the lowest ash layer. The mean bias is 0.6 km, relative to the highest ash layer, which is much less than the 3 km accuracy specification. The complicated vertical structure depicted in this scene prevents an accurate CALIOP based cloud emissivity from being calculated. Thus, the ash mass loading was not validated for this case. Direct comparisons like this will be made whenever possible.

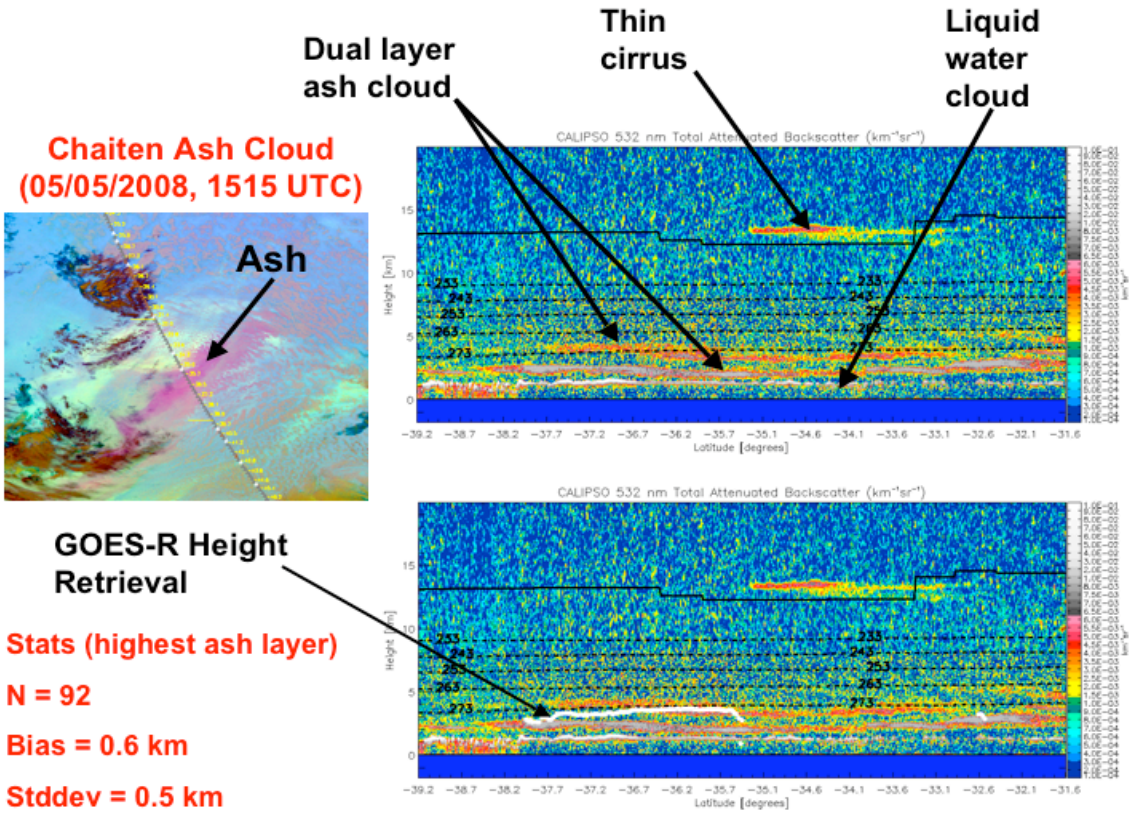

Figure 14: CALIOP observations of a complex multilayered ash cloud produced by an eruption of Chaiten (Chile) are shown along with co-located retrievals of ash cloud height produced by the GOES-R algorithm. The GOES-R height retrievals match the CALIOP data well.

5 PRACTICAL CONSIDERATIONS

5.1 Numerical Computation Considerations

The ABI-VAA employs an optimal estimation framework. Therefore it requires inversions of matrices that can under severe scenarios become ill-conditioned. Currently, these events are detected and treated as failed retrievals. In addition, the matrices have small dimensions. Thus, operations on them are not computationally expensive.

5.2 Programming and Procedural Considerations

The ABI-VAA makes heavy use of clear-sky radiative transfer calculations. Our current system computes the clear-sky atmospheric transmittances at low spatial resolution and with enough angular resolution to capture sub-grid variation path-length changes. This step is critical, as performing clear-sky atmospheric transmittance calculations for each pixel requires extensive memory and CPU time, but does not produce significantly better scientific results.

NWP data is heavily utilized in the ABI Volcanic Ash Algorithm. The algorithm can tolerate the use NWP data for forecasts ranging from 0 to 24 hours.

The ABI-VAA can provide usable results out to a viewing angle of 80 degrees (the F&PS minimum requirement is 60 degrees). The ABI-VAA is not applied to pixels that have a viewing angle greater than 80 degrees (the ash height and mass loading are set to missing in this case).

5.3 Quality Assessment and Diagnostics

The optimal estimation framework provides automatic diagnostic metrics and estimates of the retrieval error. We recommend that the error covariance matrices be monitored on at least a monthly basis. We also believe that the validation techniques described earlier, and in the ABI Volcanic Ash Product Validation Plan, be implemented on a regular basis.

5.4 Exception Handling

Prior to use, the ABI-VAA checks to make sure that each channel falls within the expected measurement range and that valid clear sky radiance and transmittance profiles are available for each channel. The ABI-VAA is only applied to a given pixel if all channels used in the algorithm contain valid data; otherwise the algorithm output is flagged as missing. The science of the volcanic ash algorithms does not allow for a graceful degradation of the products.

5.5 Algorithm Validation

Volcanic ash clouds are present infrequently relative to other types of cloud, and lidars and in-situ instruments rarely observe them. As such, volcanic ash products are very difficult to validate. Despite this challenge, it is currently possible to use spaceborne lidar observations (CALIOP) of volcanic ash and desert dust to validate the ABI volcanic ash algorithm as applied to SEVIRI or MODIS. During the GOES-R era though, it is not guaranteed that spaceborne lidar observations of ash or dust, co-located with ABI measurements, will be available, although the European Space Agency (ESA) EarthCARE mission is scheduled to coincide with the GOES-R era. The availability of spaceborne lidar observations during the GOES-R era should only pose a moderate risk to the validation of the ABI volcanic ash algorithm because the algorithm was designed to be minimally sensitive to the exact characteristics of the channels used in the algorithm. The algorithm is sensitive, however, to the accuracy of the ABI clear sky radiance calculations that are needed. Thus, one of our main focuses will be to monitor the clear sky radiance biases during ABI operations, especially early on. Finally, we are hopeful that in-situ observations via UAV's will be possible during the GOES-R era, as in-situ measurements are the ultimate direct validation source. Continued collaboration with the volcanic ash research community is critical to assure access to unique and detailed validation data sets. Please refer to the ABI Volcanic Ash Product Validation Plan Document for extensive information on pre and post launch validation plans.

6 ASSUMPTIONS AND LIMITATIONS

The following sections describe the current limitations and assumptions in the current version of the ABI-VAA

6.1 Performance

The following assumptions have been made in developing and estimating the performance of the ABI-VAA. The following lists contain the current assumptions and proposed mitigation strategies.

1. NWP data of comparable or superior quality to the current 6 hourly GFS forecasts are available. (Mitigation: Use longer-range GFS forecasts or switch to another NWP source – e.g. ECMWF).

2. Top-of-atmosphere clear sky radiances are available for each pixel and 101 level profiles of clear sky atmospheric transmittance and radiance are available at the NWP data horizontal resolution. (Mitigation: Use reduced spatial resolution top-of-atmosphere clear sky radiances. The profiles of transmittance and radiance must be present at, at least, the NWP spatial resolution and 101 vertical levels).

3. All of the static ancillary data are available at the pixel level. (Mitigation: Reduce the spatial resolution of the surface type, land mask and or coast mask).

4. The processing system allows for processing of multiple scan lines at once for application of important spatial analysis techniques. (Mitigation: No mitigation is possible).

In addition, the clear sky radiance calculations are prone to large errors, especially near coastlines, in mountainous regions, snow/ice field edges, and atmospheric frontal zones, where the NWP surface temperature and atmospheric profiles are less accurate. The impact of these errors on the ABI-VAA depends on the cloud optical depth. For optically thick clouds (infrared optical depth of about 1.0 or greater), these errors have a small impact since the difference between the observed and black cloud radiance approach zero as the cloud optical depth increases. This is not the case for optically thin clouds, where inaccurate NWP data can have serious impacts. Thus, clear sky radiance biases need to be monitored on a regular basis (~monthly).

6.2 Assumed Sensor Performance

We assume the sensor will meet its current specifications. However, the ABI-VAA will be dependent on the following instrumental characteristics.

- Unknown spectral shifts in some channels will cause biases in the clear-sky RTM calculations that may impact the performance of the ABI-VAA. Clear sky radiance biases need to be monitored throughout ABI's lifetime.

6.3 Pre-Planned Product Improvements

While development of the baseline ABI-VAA continues, we expect in the coming years to focus on the following improvement.

6.3.1 Use of 10.4-μm channel

The 10.4 μm channel is new to the world of satellite imagers. We expect to incorporate this channel into the ABI-VAA to improve volcanic ash detection and ash retrievals. We expect the GOES-R Risk Reduction projects to demonstrate its use before implementation into the operational algorithm.

7 REFERENCES

Cox, S. K., 1976: Observations of Cloud Infrared Effective Emissivity. *J.Atmos.Sci.,* **33**, 287-289.

Downing, H. D., D. Williams, 1975: Optical-Constants of Water in Infrared. *Journal of Geophysical Research,* **80**, 1656-1661.

Giraud, V., J. C. Buriez, Y. Fouquart, F. Parol, and G. Seze, 1997: Large-scale analysis of cirrus clouds from AVHRR data: Assessment of both a microphysical index and the cloud-top temperature. *J.Appl.Meteorol.,* **36**, 664-675.

Hansen, M., R. DeFries, J.R.G. Townshend, and R. Sohlberg (1998), UMD Global Land Cover Classification, 1 Kilometer, 1.0, Department of Geography, University of Maryland, College Park, Maryland, 1981-1994.

Heidinger, A. K. and M. J. Pavolonis, 2009: Nearly 30 years of gazing at cirrus clouds through a split-window. Part I: Methodology. *J.Appl.Meteorol. and Climatology*, In Press (early online release).

Inoue, T., 1987: A Cloud Type Classification with Noaa 7 Split-Window Measurements. *J.Geophys.Res.-Atmos.,* **92**, 3991-4000.

Mitchell, D. L., 2000: Parameterization of the Mie extinction and absorption coefficients for water clouds. *J.Atmos.Sci.,* **57**, 1311-1326.

Neal, C. A., R. G. McGimsey, C. A. Gardner, M. L. Harbin, and C. J. Nye, 1994: Tephra-fall deposits from 1992 eruptions of Crater Peak, Mount Spurr Volcano, AK: A preliminary report on distribution, stratigraphy, and composition. The 1992 eruptions of Crater Peak vent, Mount Spurr volcano, Alaska, U.S. Geological Survey Bulletin 2139, 65-79.

Parol, F., J. C. Buriez, G. Brogniez, and Y. Fouquart, 1991: Information-Content of Avhrr Channels 4 and 5 with Respect to the Effective Radius of Cirrus Cloud Particles. *J.Appl.Meteorol.,* **30**, 973-984.

Pavolonis, M. J., W. F. Feltz, A. K. Heidinger, and G. M. Gallina, 2006: A daytime complement to the reverse absorption technique for improved automated detection of volcanic ash. *J.Atmos.Ocean.Technol.,* **23**, 1422-1444.

Pavolonis, M. J., 2009a: Advances in extracting cloud composition information from spaceborne infrared radiances: A robust alternative to brightness temperatures. Part I: Theory. Submitted to *J. Atmos. Sci.*

Pavolonis, M. J., 2009b: Advances in extracting cloud composition information from spaceborne infrared radiances: A robust alternative to brightness temperatures. Part II: Proof of concept. Submitted to *J. Atmos. Sci.*

Pollack, J. B., O. B. Toon, and B. N. Khare, 1973: Optical Properties of some Terrestrial Rocks and Glasses. *Icarus,* **19**, 372-389.

Prata, A. J., 1989: Observations of volcanic ash clouds in the 10-12-micron window using AVHRR/2 Data. *Int.J.Remote Sens.,* **10**, 751-761.

Prata, A. J. and I. F. Grant, 2001: Retrieval of microphysical and morphological properties of volcanic ash plumes from satellite data: Application to Mt Ruapehu, New Zealand. *Q. J. R. Meteorol. Soc.*, **127**, 2153-2179.

Rodgers, C. D., 1976: Retrieval of atmospheric temperature and composition from remote measurements of thermal radiation. *Reviews of Geophysics and Space Physics*, **14**, 609-+.

Roush, T., J. Pollack, and J. Orenberg, 1991: Derivation of Midinfrared (5-25 Mu-M) Optical-Constants of some Silicates and Palagonite. *Icarus,* **94**, 191-208.

Seemann, S. W., E. E. Borbas, R. O. Knuteson, G. R. Stephenson, and H. Huang, 2008: Development of a global infrared land surface emissivity database for application to clear sky sounding retrievals from multispectral satellite radiance measurements. *J.Appl.Meteorol.Climatol.,* **47**, 108-123, doi:10.1175/2007JAMC1590.1.

Van de Hulst, H. C., 1980: *Multiple Light Scattering, Tables, Formulas, and Applications.* Vol. 2. Academic Press, 739 pp.

Wen, S. and W. I. Rose, 1994: Retrieval of sizes and total masses of particles in volcanic ash clouds using AVHRR bands 4 and 5. *J. Geophys. Res.*, **99**, 5421-5431.

Warren, S. G., R. E. Brandt, 2008: Optical constants of ice from the ultraviolet to the microwave: A revised compilation. *J.Geophys.Res.-Atmos.,* **113**, D14220, doi:10.1029/2007JD009744.

Yang, P., H. L. Wei, H. L. Huang, B. A. Baum, Y. X. Hu, G. W. Kattawar, M. I. Mishchenko, and Q. Fu, 2005: Scattering and absorption property database for nonspherical ice particles in the near- through far-infrared spectral region. *Appl.Opt.,* **44**, 5512-5523.

Zhang, H., W. P. Menzel, 2002: Improvement in thin cirrus retrievals using an emissivity-adjusted CO2 slicing algorithm. *J.Geophys.Res.-Atmos.,* **107**, 4327, doi:10.1029/2001JD001037.

Zhang, P., N. Lu, X. Hu, and C. Dong, 2006: Identification and physical retrieval of dust storm using three MODIS thermal IR channels. *Global Planet.Change,* **52**, 197-206, doi:10.1016/j.gloplacha.2006.02.014.